

https://dspace.org/

Alveolar macrophages from persons with HIV mount impaired TNF signaling networks to Mtuberculosis infection

Khanyisile Kgoadi; Prashant Bajpai; Chris C Ibegbu; Hedwin K Dkhar; Ana B Enriquez ...

NATURE PUBLISHING GROUP
https://hdl.handle.net/10539/48557
WOS

Downloaded from a DSpace repository. https://dspace.org/

nature communications

Article

https://doi.org/10.1038/s41467-025-57668-y

Alveolar macrophages from persons with HIV mount impaired TNF signaling networks to *M. tuberculosis* infection

Received: 10 June 2024

Accepted: 27 February 2025

Published online: 10 March 2025

Check for updates

Khanyisile Kgoadi[1,5], Prashant Bajpai[1,5], Chris C. Ibegbu[1], Hedwin Kitdorlang Dkhar[1], Ana Beatriz Enriquez[1], Stanzin Dawa[1], Sushma K. Cribbs[2,3,6] & Jyothi Rengarajan[1,4,6]

People living with HIV (PLWH) have an increased risk for developing tuberculosis after *M. tuberculosis* infection, despite anti-retroviral therapy (ART). To delineate the underlying mechanisms, we conducted single cell transcriptomics on bronchoalveolar lavage cells from PLWH on ART and HIV uninfected healthy controls infected with *M. tuberculosis* ex vivo. We identify an M1-like proinflammatory alveolar macrophage subset that sequentially acquires TNF signaling capacity in controls but not in PLWH. Cell-cell communication analyses reveal interactions between M1-like macrophages and effector memory T cells within TNF superfamily, chemokine, and costimulatory networks in the airways of controls. These interaction networks were lacking in PLWH infected with *M. tuberculosis*, where anti-inflammatory M2-like alveolar macrophages and T regulatory cells dominated along with dysregulated T cell signatures. Our data support a model in which impaired TNF-TNFR signaling, M2-like alveolar macrophages and aberrant macrophage-T cell crosstalk, lead to ineffective immunity to *M. tuberculosis* in PLWH on ART.

Tuberculosis (TB), caused by lung infection with *Mycobacterium tuberculosis* (Mtb), is the leading cause of mortality in people living with human immunodeficiency virus (HIV) and accounts for an estimated 6.3% of TB cases and 167,000 deaths in 2022 alone[1]. Globally, persons living with HIV (PLWH) are about 20-fold more likely to develop TB compared to those living without HIV[2–4]. Antiretroviral therapy (ART) has led to significant improvements in clinical outcomes for PLWH by decreasing HIV viral loads to near undetectable levels and restoring CD4 T cell counts[5,6]. However, despite successful ART treatment, PLWH on ART continue to have a 4-fold higher risk of developing TB compared to HIV uninfected persons[7]. The higher rates of TB and other opportunistic respiratory infections in PLWH on ART, despite restoration of CD4:CD8 ratios, suggest that pulmonary immune responses in PLWH remain defective and are unable to provide protection against respiratory pathogens such as Mtb.

Alveolar macrophages (AMs) are the major immune cell type present in the upper respiratory tract. AMs play critical roles in host defense by maintaining homeostasis in lung tissue, where they are prevented from being continuously activated by receiving inhibitory signals[8–11] and are the first cells to encounter and become infected by Mtb[12–14]. Upon phagocytosis of microbes, AMs rapidly mount proinflammatory and antimicrobial responses and shape the nature of protective T cell immunity[15,16]. However, we have a poor understanding of whether AMs from PLWH are compromised in mounting immune defense against Mtb. A number of observational studies and clinical trials have shown that systemic residual inflammation persists in PLWH on ART despite suppressed viral loads[17–19]. AMs from PLWH have been

[1]Emory Vaccine Center, Emory National Primate Center, Emory University, Atlanta, GA, USA. [2]Division of Pulmonary, Allergy, Critical Care & Sleep, Department of Medicine, Emory University School of Medicine, Atlanta, GA, USA. [3]Department of Veterans Affairs, Atlanta, GA, USA. [4]Division of Infectious Diseases, Department of Medicine, Emory University School of Medicine, Atlanta, GA, USA. [5]These authors contributed equally: Khanyisile Kgoadi, Prashant Bajpai. [6]These authors jointly supervised this work: Sushma K Cribbs, Jyothi Rengarajan. e-mail: skomaku@emory.edu; jrengar@emory.edu

found to harbor proviral HIV DNA and even HIV RNA, regardless of the presence of detectable plasma HIV RNA[20]. Moreover, PLWH showed lower levels of reduced glutathione and increased H_2O_2 and NADPH oxidase enzymes[21] in bronchoalveolar lavage (BAL) compared to persons without HIV, suggesting heightened oxidative stress in the lungs of PLWH. Interestingly, AMs from PLWH on ART infected with Mtb were reported to have limited changes in chromatin accessibility compared to persons without HIV, suggesting that AMs from PLWH have altered epigenetic responses to Mtb infection[22]. We sought to further investigate AM functions in PLWH via high-dimensional flow cytometric immunophenotyping and single cell transcriptional profiling of BAL cells from PLWH and HIV-uninfected healthy controls (HC), both at baseline and in response to ex vivo Mtb infection.

Here, we show that PLWH and HC exhibit significant differential gene expression across multiple myeloid and lymphoid subsets in their airways following Mtb infection. We identify an M1-like AM subset in HC that sequentially acquires TNF signaling capacity following Mtb infection and promotes crosstalk with CD4 and CD8 effector memory T cell networks. In contrast, PLWH induce IL-10-expressing M2-like AM subsets upon Mtb infection and promote interactions with the immunosuppressive receptor CD200R. Overall, our studies suggest a model in which poor AM-T cell crosstalk in the lung compartments of PLWH on ART leads to aberrant immune responses to Mtb in PLWH.

Results

Comparable distribution of immune cell populations in bronchoalveolar compartments from people living with HIV and healthy controls

To characterize the immune cells in the bronchoalveolar compartments of PLWH on ART and HIV-uninfected persons and to study their responses to Mtb infection, we enrolled two groups of study participants: PLWH on ART and HIV-uninfected healthy controls (HC). We collected bronchoalveolar lavage fluid (BALF) samples from PLWH on ART ($n = 7$) and HC ($n = 9$). Table 1 shows the demographic characteristics of study participants enrolled in the study. All PLWH were stable on ART with median CD4 counts of 493 cells/ul; interquartile range (IQR) (271–833); and all the participants had undetectable HIV viral load. BAL cells isolated from the BALF of participants from HC and PLWH on ART were used for immunophenotyping at baseline and infected with Mtb for single-cell transcriptomics (10X Genomics) and analysis of immune function by high-dimensional flow cytometry (Fig. 1A).

To determine the composition of immune cell populations in BAL cells from HC and PLWH on ART, we performed comprehensive immunophenotyping using multiparameter flow cytometry (Fig. 1B and Supplementary Fig. 1). Alveolar macrophages (AMs) were the predominant immune cells in BAL cells from both groups, with a median of 78.6% (IQR: 67.2–90.0) in HC and 75.1% (IQR: 61.5–76.1) in PLWH, as expected (Supplementary Table 1). Other notable immune cell types included CD4 T cells, CD8 T cells, monocytes, neutrophils, and epithelial cells; however, we did not observe any significant differences in the frequencies of these cell types between the two groups (Fig. 1C).

Table 1 | Clinical characteristics of healthy controls (HC) and people living with HIV (PLWH)

	HC ($n = 9$)	PLWH ($n = 7$)
Age (median, range)	60 (30–73)	58 (49–66)
Male %	88.88% ($n = 8$)	100% ($n = 7$)
Female %	11.11% ($n = 1$)	0%
Smoking status		
• Non-smoker	4	4
• Smoker	3	2
• Ex-smoker	2	1
Viral Load	NA	Undetected
CD4 Count (median, range)	NA	493 (271–833)

Single cell transcriptional profiling reveals global transcriptional changes across multiple cell types in response to Mtb

We sought to investigate the transcriptional responses of AMs and other BAL cells from PLWH and HCs to ex vivo infection with Mtb by carrying out single cell transcriptomic profiling (scRNA-seq;10X Genomics) at baseline (no infection) and after infection with Mtb H37Rv at an MOI of 2 for 4 h. After this time, cells were collected for bacterial enumeration and processing for ScRNA-seq. After plating intracellular Mtb, colony forming units (CFUs) were 1×10^6 (IQR: 0.5×10^6–1.37×10^6) in HC and 1.25×10^6 (IQR: 0.4×10^6–2.12×10^6) CFU/ml in PLWH, demonstrating that bacterial loads were comparable between the two groups. After alignment and preprocessing of the ScRNAseq data, we obtained an average of 3362 cells per sample, yielding a total of 57,160 cells. Upon mapping sequences to the Human Primary Cell Atlas reference dataset, we identified 12 distinct cell populations (Supplementary Fig. S2A): alveolar macrophages (*MACRO*$^+$, *CD68*$^+$, *FCGR3A*$^+$), monocyte derived macrophages (*MACRO*$^+$, *SIGLEC5*$^-$), neutrophils (*S100A8*$^+$, *S100A9*$^+$), dendritic cells (*CD1C*$^+$, *CD207*$^+$), monocytes (*LYZ*$^+$), CD4 T cells (*CD3D*$^+$, *CD3E*$^+$, *CD4*$^+$), CD8 T cells (*CD3D*$^+$, *CD3E*$^+$, *CD8A*$^+$), gamma delta T cells (*CD3E*$^+$, *CD3G*$^+$), T-regulatory cells (*FOXP3*$^+$), B cells (*MA4A1*$^+$, *CD79A*$^+$), NK cells (*GNLY*$^+$, *PRF1*$^+$) and epithelial cells (*MUC5AC*$^+$). Cell types projected in two dimensions using Uniform Manifold Approximation and Projection (UMAP) are shown in Fig. 2A. Cell populations were further validated using canonical gene expression markers (Supplementary Fig. 2A). Overall, the cell types identified by scRNA-seq are consistent with our flow cytometry data (Fig. 1B and Supplementary Fig. 2B). Notably, after Mtb infection, in AMs from both HC and PLWH, we identified AM clusters that were distinct from the AM clusters in the Mtb-uninfected groups (Supplementary Fig 2C), demonstrating that Mtb infection leads to significant changes within the AM compartment.

We next sought to identify genes whose expression varied significantly across the four groups (HC, PLWH, HC + Mtb, and PLWH + Mtb) and across the different cell types. A heatmap of the top differentially expressed genes indicates that the greatest differences between PLWH and HC occurred following Mtb infection, across multiple cell types (Fig. 2B). We then performed differential gene expression analysis to identify genes that were upregulated or downregulated in PLWH versus HC, in the presence or absence of Mtb, across all cell subsets. Using cutoff criteria of foldchange greater than 1.3 or less than −1.3 and adjusted p value < 0.05, we found a total of 1105 differentially expressed genes (DEGs) in HC + Mtb compared to HC and 902 DEGs in PLWH + Mtb compared to PLWH group (Fig. 2C). Of the total DEGs, 710 were common between the HC + Mtb and PLWH + Mtb, while 395 and 192 genes were unique to HC + Mtb and PLWH + Mtb respectively (Fig. 2C and Supplementary Fig. 2D). Pathway enrichment analysis of common and unique DEGs across all cell types indicated that while both HC and PLWH showed positive enrichment of multiple pathways upon Mtb infection, including TNF signaling via NFκB, and IL-1 signaling, enrichment of many of these these pathways were lower in PLWH + Mtb compared to HC + Mtb (Fig. 2D).

Altered alveolar macrophage and T cells profiles in PLWH on ART following Mtb infection

To further evaluate how Mtb infection impacts the transcriptional profiles of the main innate and adaptive cell types from PLWH and HC, we compared the DEGs between PLWH and HC in the following major cell types: AMs, monocytes, CD4 T, CD8 T, and NK cells, at both baseline and after Mtb infection. Using cutoff criteria of foldchange ≥ 1.3 or ≤−1.3 and adjusted p value < 0.05, we found 50 genes to be

https://doi.org/10.1038/s41467-025-57668-y

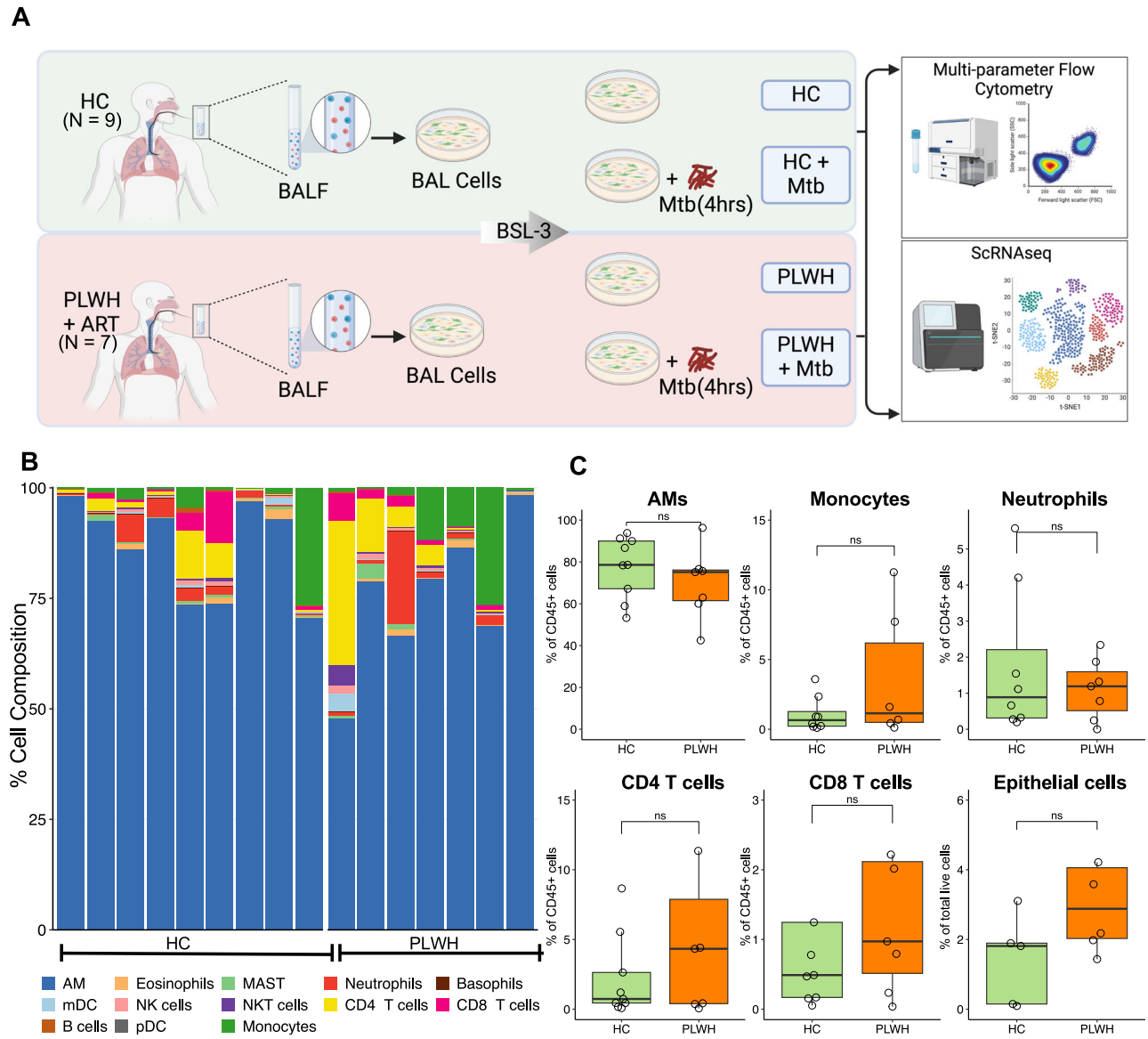

Fig. 1 | Cellular distribution of bronchoalveolar lavage (BAL) cells. A Overview of experimental methodology. Briefly, BAL fluid was collected through bronchoscopy from HCs ($n = 9$) and PLWH ($n = 7$). BAL fluid was processed to obtain BAL cells, portion of which were used for immunophenotyping and intracellular cytokine staining (ICS) at baseline. Parallelly, BAL cells from HC and PLWH were infected with Mtb for 4 h and processed further for flow cytometry, ICS, and ScRNAseq. Created in BioRender. Bajpai, P. (2025) https://BioRender.com/u96g032 (**B**) Distribution of immune cells in BAL identified through flow cytometry. Each bar represents one subject, and color shows different cell types. **C** Boxplot shows distribution of major cell types in the BAL between HC ($n = 9$) and PLWH ($n = 7$) identified through immunophenotyping. Individuals are represented as dots. The following parameters are shown: minimum, lower quartile, median, upper quartile, and maximum. Two-sided Student's *t*-test was used to compare difference between sample means. ns; p value > 0.05. **A** was generated using BioRender.

upregulated, and 45 genes downregulated in AMs from PLWH compared to HC at baseline as shown in the alluvial plots in Fig. 3A. Upon Mtb infection, the number of DEGs in AMs increased to 103 upregulated and 206 downregulated (Fig. 3A). Similar trends were observed in CD4 T cells, CD8 T cells and NK cells (Fig. 3A). Other cell subsets either showed minimal changes in response to Mtb (DCs and monocytes) or had no significant DEGs (γδT, T_{reg}, Fig. 3A). Focusing on the DEGs post-Mtb infection, we found that AMs from PLWH downregulated multiple cytokine and chemokine genes relative to HC, such as *IL-6, TNF, IL1A, IL23A, IL1B, CCL4/5, CXCL1/3/8* and the antioxidant *SOD2*, suggesting that AMs from PLWH on ART are unable to mount robust pro-inflammatory and antimicrobial responses to Mtb (Fig. 3B). Moreover, CD4 T cells, CD8 T cells and NKs cells from PLWH + Mtb showed signatures of immune activation and heightened inflammation (*HLA-DRA/DRB, TNF, CCL4*) relative to HC + Mtb and downregulation of *GZMA, GZMB, and GNLY* which encode granzyme A, B and granulysin, respectively, suggesting blunted cytotoxic T cell responses in PLWH (Fig. 3B).

To identify pathways that differ between innate and adaptive immune cells from PLWH + Mtb *versus* HC + Mtb, we performed gene set enrichment analysis (GSEA) using Hallmark and Reactome reference datasets. Host pathways corresponding to pro-inflammatory cytokine signaling, such as TNF, IL-1, IL-6, IFN-α, and IFN-γ, were significantly lower in AMs, DCs, and monocytes from PLWH + Mtb compared to HC + Mtb (Fig. 3C) following Mtb infection, along with diminished IL-4/13 and IL-10. These data suggest that in contrast to HC, which successfully mounts a robust and balanced innate inflammatory response, PLWH are defective in

https://doi.org/10.1038/s41467-025-57668-y

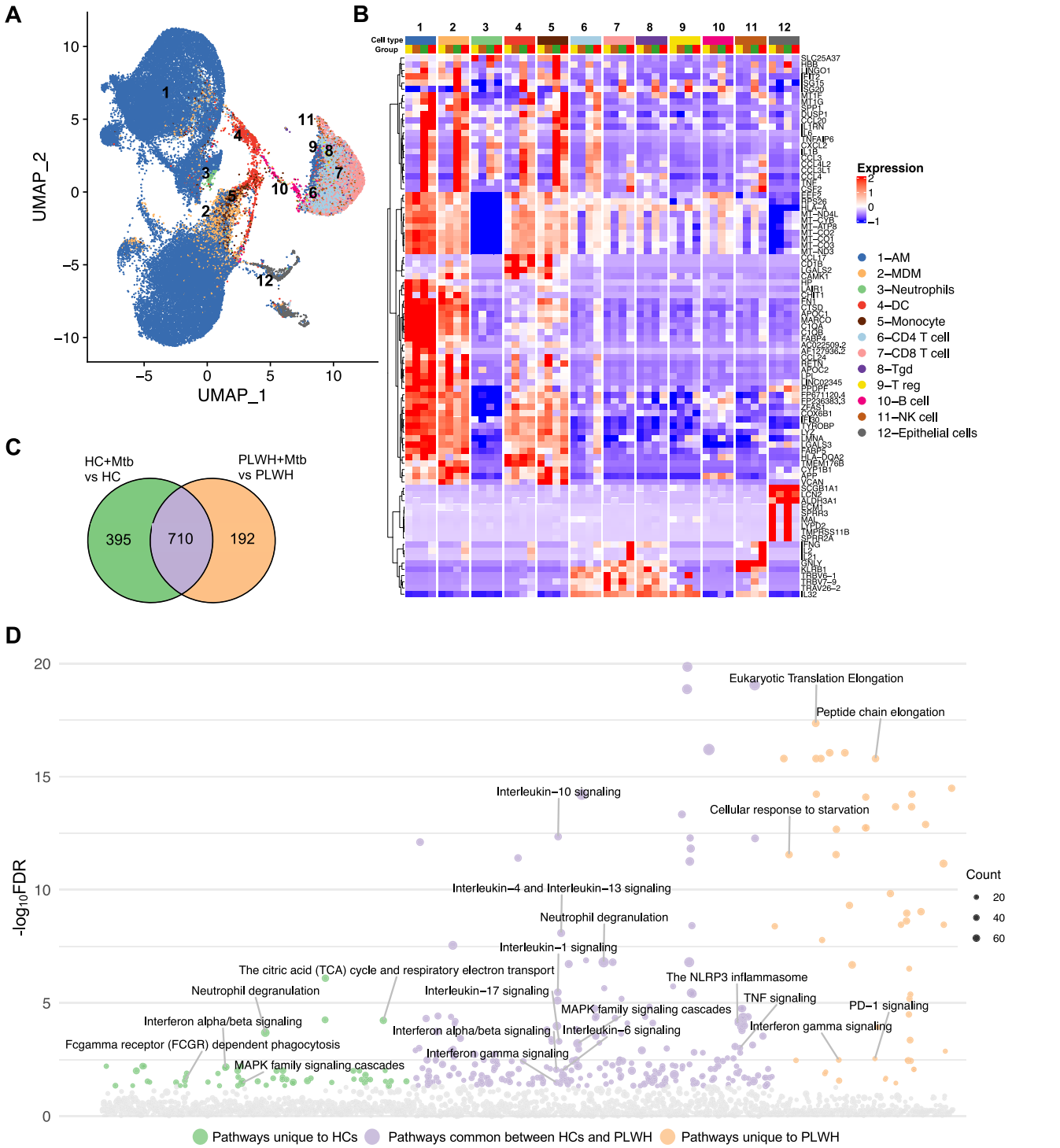

Fig. 2 | Landscape of transcriptional responses to Mtb in HC and PLWH. **A** Concatenated UMAP of HC ($n = 5$), PLWH ($n = 3$), HC + Mtb ($n = 5$), and PLWH + Mtb ($n = 4$) shows the annotated cell types in the BAL cells. **B** Heatmap of top 10 variable genes per group. Color represents the Z-scores (row normalization) of the average expression of each gene for each group and cell type. Genes with high expression are shown in red and low expression in blue. Genes in each row were clustered using hierarchal clustering by farthest neighbor method. **C** Venn diagram of differentially expressed genes (DEGs) between the HC + Mtb compared to HC and PLWH + Mtb compared to PLWH. **D** Manhattan plot shows the pathways enriched in unique DEGs in HC + Mtb vs HC (green), unique DEGs in PLWH + Mtb vs PLWH (orange), and common DEGs between HC + Mtb vs HC and PLWH + Mtb vs PLWH (violet). *Y*-axis shows the FDR corrected *p* value obtained from the pathway enrichment analysis, and size of each bubble shows the count of genes that overlapped with reference pathway. *P* value was estimated using overrepresentation analysis in R package enrichR.

responding to Mtb infection. This is supported by the lack of upregulation of glycolysis in PLWH, where genes involved in oxidative phosphorylation (OXPHOS), electron transport, and tricarboxylic acid (TCA) cycle metabolism were enriched in innate cell subsets (Fig. 3C). In contrast, OXPHOS and TCA metabolic genes were lower in CD4 and CD8 T cells from PLWH along with lower IFN-α and IFN-γ signaling (Fig. 3C), suggesting poorly functional T cells in lung compartments of PLWH.

https://doi.org/10.1038/s41467-025-57668-y



Fig. 3 | Differential gene expression analysis of major cell types in BAL in HC and PLWH in response to Mtb infection. A Alluvial plot shows the change in number of differentially expressed genes between PLWH vs HC and PLWH + Mtb vs HC + Mtb. Up-regulated genes are shown in red, while downregulated genes are shown in blue. Only the cell types with significant number of DEGs are shown. **B** MA-plot shows the gene expression profile of PLWH + Mtb vs HC + Mtb in major cell types. *X*-axis shows the normalized log2 mean expression of each gene, and *y*-axis shows the log2 foldchange. Up-regulated genes are shown in red, while down-regulated genes are shown in blue. **C** Bubble plot shows the enriched pathways between PLWH + Mtb and HC + Mtb obtained from gene set enrichment analysis (GSEA). Up-regulated pathways in PLWH + Mtb vs HC + Mtb are shown in red, while downregulated pathways are shown in blue. The size of the bubble represents the size of the reference pathway (i.e., number of genes which compose that pathway).

https://doi.org/10.1038/s41467-025-57668-y

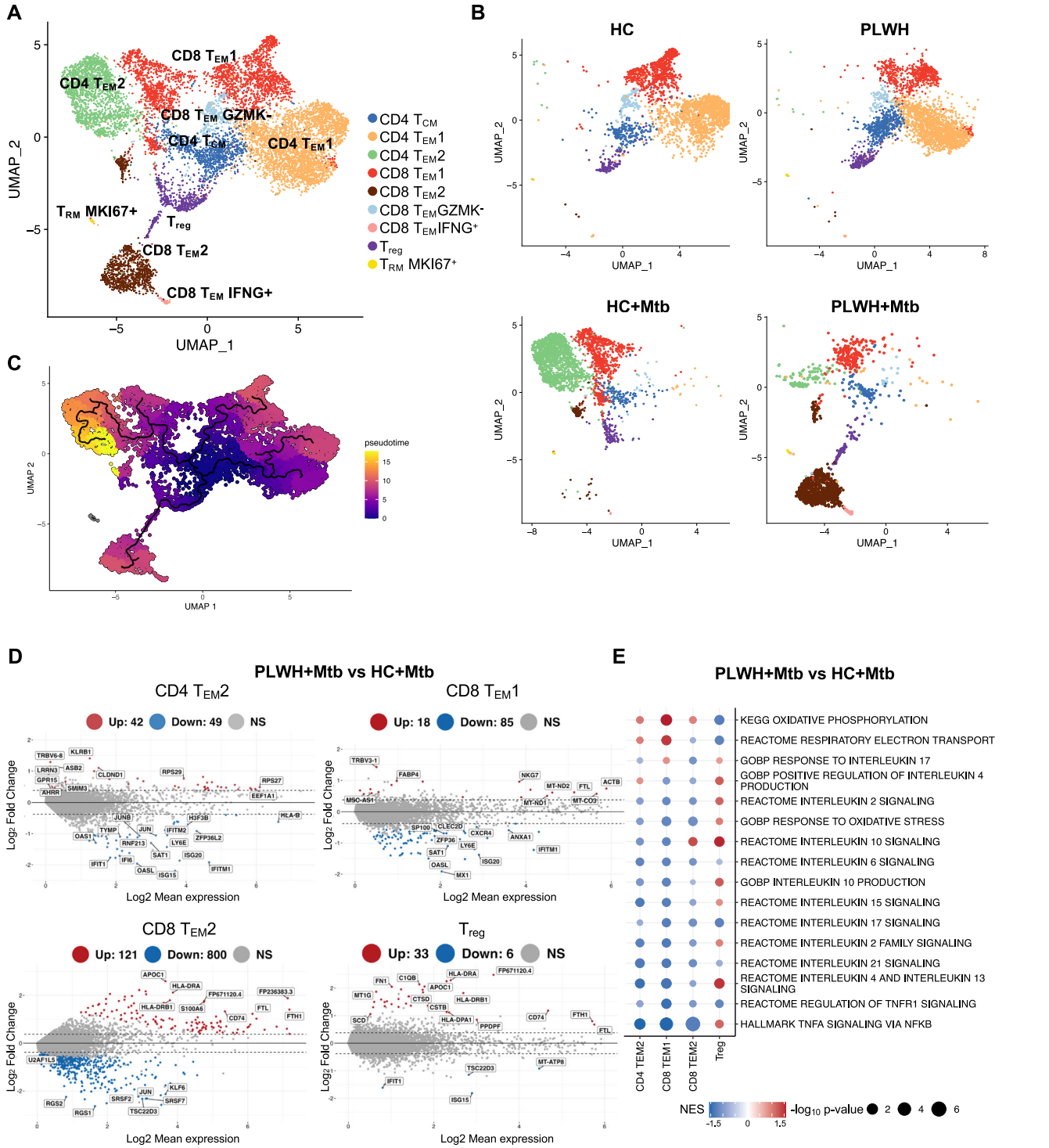

Fig. 4 | Overview of T cell transcriptional response to Mtb infection in HC and PLWH. A Concatenated UMAP of HC ($n = 5$), PLWH ($n = 3$), HC + Mtb ($n = 5$), and PLWH + Mtb ($n = 4$) shows various T-cell subsets annotated using canonical reference markers. **B** UMAP of T-cell subsets identified in HC, PLWH, HC + Mtb, and PLWH + Mtb groups. **C** Pseudotime trajectory of T cell subsets inferred using Monocle 3. Cells were colored by pseudotime. **D** MA-plot shows the gene expression profile of PLWH + Mtb vs HC + Mtb in T cell subsets. *X*-axis shows the normalized log2 mean expression of each gene, and *y*-axis shows the log2 foldchange. Up-regulated genes are shown in red, while downregulated genes are shown in blue. Only the subsets with enough DEGs are shown. **E** Bubble plot shows the enriched pathways between PLWH + Mtb and HC + Mtb obtained from gene set enrichment analysis (GSEA) in various T cell subsets. Up-regulated pathways in PLWH + Mtb vs HC + Mtb are shown in red, while downregulated pathways are shown in blue. The size of the bubble represents the −log10 *p* value. The larger the size of the bubble, lower the *p* value. *P* value and enrichment score are obtained from GSEA analysis using R package fgsea.

T cell subsets in the airways of PLWH reflect heightened immune activation and dysregulation

We characterized the T cell subsets present in the bronchoalveolar compartments of PLWH and HC at baseline and assessed changes following infection with Mtb. We identified multiple subsets of CD4 and CD8 T cells as shown in the concatenated UMAP plot of all 4 groups (Fig. 4A and Supplementary Fig. 3A). Figure 4B shows that uninfected BAL cells from PLWH and HC both harbored similar CD4 T

central memory (T_{CM}), CD4 and CD8 T effector memory (T_{EM}) and T_{reg} subsets. However, Mtb exposure led to shifts in the T_{CM} and T_{EM} populations in each group, with a distinct CD4 T_{EM2} cluster in HC that was absent in PLWH, and a CD8 T_{EM2} cluster in PLWH that was absent in HC (Fig. 4A). These population shifts were not associated with cell death as cell viability and percentage of mitochondrial content were observed to be similar before and after Mtb infection (Supplementary Fig. 3B, C). Pseudotime and GSEA analysis suggest that upon Mtb infection, resting CD4 and CD8 T cells in HC likely differentiate into effector memory CD4 T cells with an antimicrobial gene expression profile (CD4T_{EM2}), and CD8 T cells with cytotoxic profiles (CD8 T_{EM1}), including a granzyme K-expressing CD8 T cell subset (CD8 T_{EM} GZK+) (Fig. 4C). Importantly, these effector memory CD4 and CD8 T cell subsets are not present in PLWH; instead, Mtb infection leads to differentiation into a unique subset of effector memory CD8 T cells (CD8 T_{EM2}), and a small IFN-γ-expressing CD8 effector memory subcluster, both of which are absent in HC (Fig. 4C).

To further understand the functional capacity of these T cell subsets, we analyzed the DEGs that differed the most between PLWH + Mtb and HC + Mtb. Figure 4D, E shows that multiple genes within the effector memory CD4 T_{EM2} and CD8 T_{EM1} subsets were downregulated in PLWH compared to HC, and GSEA shows that these downregulated genes corresponded to IL-2, IL-6, IL-10, IL-15, IL-17, IL-21 and TNFR1 signaling pathways, suggesting substantially reduced CD4 and CD8 T cell functionality in PLWH. Further, effector memory CD8 T_{EM2} subsets present in PLWH significantly upregulated immune activation genes (e.g., *HLADRA/B1*) and were enriched for IL-10 signaling pathways, along with reduced cytokine signaling pathways (Fig. 4D, E). Finally, T_{regs} from PLWH + Mtb also displayed gene signatures of hyper immune activation and were significantly enriched for signaling pathways corresponding to anti-inflammatory IL-10 and IL-4/IL-13 cytokine signaling, suggesting that T_{regs}, preferentially induced in PLWH, may contribute to skewing away from a proinflammatory milieu and towards an immunosuppressive or anti-inflammatory lung microenvironment (Fig. 4D, E).

Cell-cell communication networks reflect divergent immune responses to Mtb in PLWH versus HC

To identify cell-cell communication networks operant in PLWH versus HC following Mtb infection, we used CellChat, which uses a comprehensive curated database of ligand-receptor interactions and network analysis to predict communication probabilities for different pathways from single cell transcriptomics data. We calculated the relative flow of information for each pathway within the database by aggregating communication probabilities across all cell types for each pathway. A higher relative information flow score indicates increased communication between cell subsets. CellChat predicted significant induction of IL-6, IL-1, TNF signaling networks, CD86 costimulatory, and MHC-I signaling pathways in HC + Mtb (Fig. 5A). However, these interaction networks were either absent or significantly lower in PLWH + Mtb. Notably, further analysis predicted crosstalk primarily between AMs and lymphocytes in HC infected with Mtb (Fig. 5B) within costimulatory and TNFSF-TNFRSF member signaling networks: TNFRSF1A/1B (TNF), TNFRSF13 (APRIL), and TNFRSF13B (BAFF). The TNF signaling network, which involves interaction between TNF and TNFRSF1A/1B, was predicted to be the strongest with the highest number of edges (represented by thicker lines) connecting AMs to CD4 T cells as well as other T cell and innate cell types (Fig. 5B, top panel). Interestingly, AMs were also central to the anti-inflammatory cell-cell communication networks that dominated in PLWH + Mtb compared to HC + Mtb, such as CD39 and LIGHT (TNFRSF14), as shown in Fig. 5A, B (bottom panel). The predominance of LIGHT in PLWH over the more proinflammatory TNF, APRIL, and BAFF signaling networks seen in HC following Mtb infection suggests that TNFSF networks are dysregulated in PLWH and likely hinder effective host defense against Mtb infection.

Impaired TNF-TNFR signaling networks in alveolar macrophages from PLWH

Since our data highlighted defective inflammatory responses to Mtb in PLWH, in particular, TNFSF-TNFRSF signaling pathways, we sought to infer the strength of inflammatory activity across each immune cell type present in BAL. We calculated pathway scores for inflammatory response pathways that were found to be downregulated in PLWH + Mtb compared to HC + Mtb (Fig. 6A, left). The pathway activity score for combined inflammatory response pathways was significantly lower in PLWH + Mtb compared with HC + Mtb. Similar results were seen for the TNF-TNFR signaling pathway (Fig. 6A, right), with AMs being the dominant contributors to inflammatory and TNF signaling pathways (Fig. 6A). To assess the TNF-TNFR signaling pathways more closely in AMs from PLWH and HC, we overlayed the fold changes of all genes involved in the TNF signaling pathway obtained from the KEGG database. Figure 6B shows that several genes within these pathways were lower in PLWH + Mtb compared to HC + Mtb. These genes include *NFKB, IKBA, AKT, MKK3, TRAF1, and JUN*. We also observed significantly lower expression of genes downstream of TNFR1 that encode IL-6, IL-1β, chemokines involved in leukocyte recruitment (CCL20, CXCL1, CXCL2, CXCL3, and CXCL5), transcription factors (Ap1, c-Fos, c-Jun), inflammatory mediators (PtgS2) and negative regulators of intracellular signaling (Tnfaip3). In contrast, *CCL2*, associated with chronic immune activation in PLWH on ART, was upregulated (Fig. 6C). To validate these data at the protein level, we quantified the levels of multiple cytokines from the supernatants of Mtb-infected BLCs from PLWH and HC using multiplex ELISAs. Several proinflammatory cytokines were significantly higher in HC compared to PLWH, including TNF, IL-6, IL-1β, and GM-CSF (Fig. 6C). Overall, these data show that AMs from PLWH are defective in mounting TNF and downstream signaling pathways.

Impaired induction of M1-like AMs and TNF signaling in PLWH on ART following Mtb infection

To further dissect AM functions in response to Mtb in HC versus PLWH, we asked which specific AM subpopulations contribute to the differential inflammatory responses in the two groups. Using Seurat clustering, we identified 5 distinct transcriptional subclusters of AMs (AM1 to AM5; Fig. 7A–C). Of these, subclusters AM2, AM3, and AM4 were prominent after Mtb infection in both HC and PLWH (Fig. 7B), while the AM1 cluster, which displayed a resting cell signature, was present mostly at baseline in both groups. The AM5 subcluster, which co-expressed lymphocyte markers, was excluded from subsequent analyzes. Interestingly, the AM3 subcluster displayed an activated, strongly proinflammatory M1-like signature which included *NFKBIA*, *IL1B, IL1RN, IL-6, TNF*, chemokine genes (*CXCL2, CXCL3, CXCL5, CXCL8, CCL3, CCL4, CCL20)* and the antimicrobial gene superoxide dismutase 2 (*SOD2*; Fig. 7C–E). The AM2 subcluster also shared many of these proinflammatory genes, but at lower levels than AM3, and had poor upregulation of NFκB signaling, suggesting a less-activated intermediate AM phenotype (Fig. 7D). The AM4 subcluster, which was enriched in PLWH compared to HC post Mtb infection, displayed a unique transcriptional signature that lacked expression of proinflammatory genes but expressed genes that contribute to anti-apoptotic and anti-inflammatory responses (*BCL2, AKT3, SMAD2*; Fig. 7D). A GSEA plot of the four subsets (Fig. 7E) confirms the distinct gene expression patterns for each AM subset: AM1 exhibit a quiescent metabolic state, the M1-like proinflammatory AM3 subset show potent TNF signaling via NFκB activation, and AM4 subsets upregulate TGF-β family signaling and cholesterol storage pathways.

To better understand the relationship between the different AM subpopulations that develop following Mtb infection in HC and PLWH, we conducted pseudotime analysis to infer the pseudotemporal trajectories of the AM subsets and their underlying gene expression programs. Pseudotime analysis indicates that the

https://doi.org/10.1038/s41467-025-57668-y

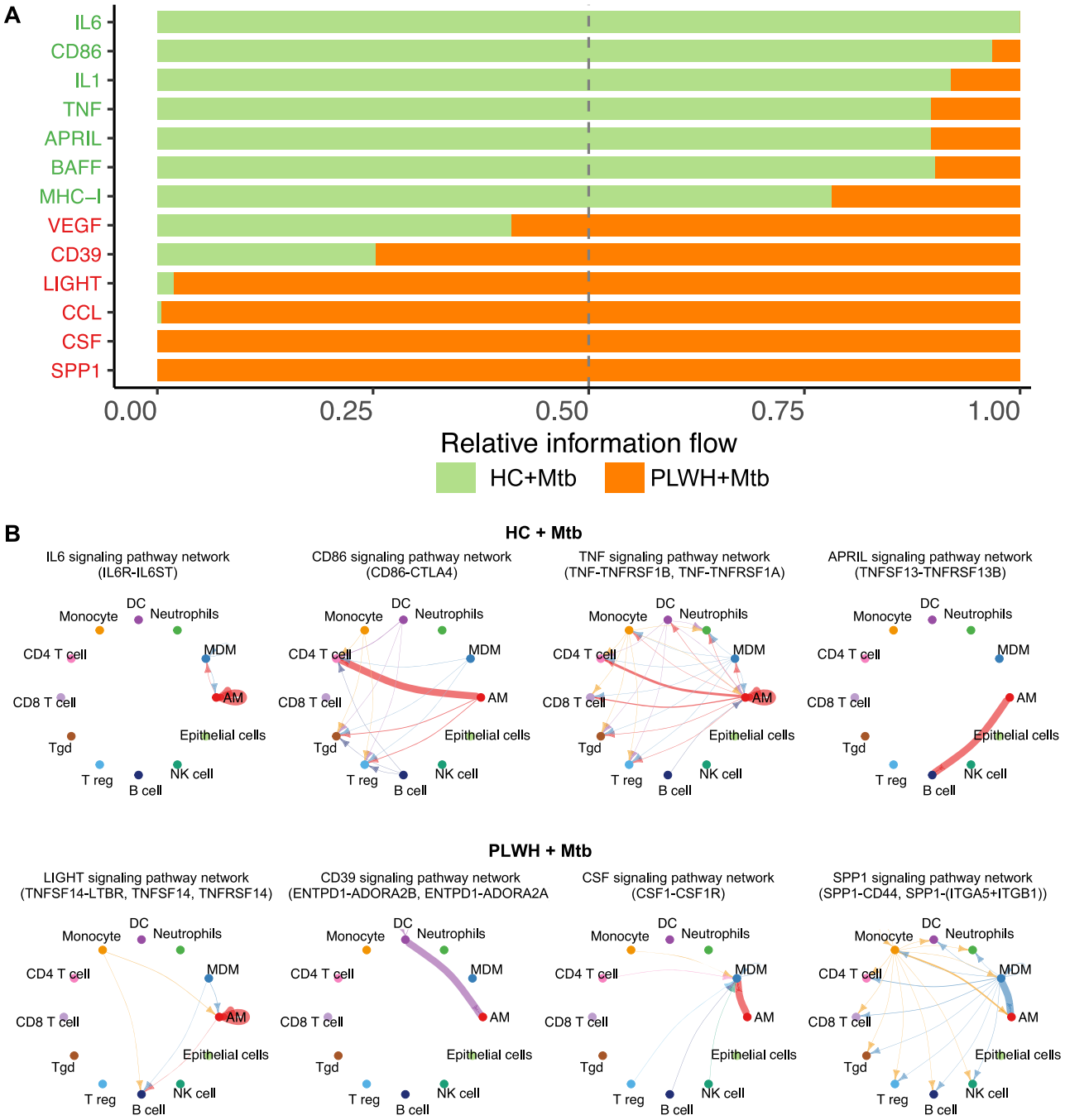

Fig. 5 | Cell-cell communication networks in PLWH in response to Mtb infection. A Figure shows the strength of cell-cell communication of significant pathways in HC + Mtb and PLWH + Mtb groups. *X*-axis shows the relative flow of information obtained from the sum of cumulative probabilities between interacting cell types and then scaled from 0 to 1. Higher value indicated higher ligand-receptor interaction between cells in each pathway. **B** Cell-cell communication network shows the putative interactions between ligand and receptor pairs. The arrow indicates the directionality of interaction, and the width of the edge indicates the strength of communication.

AM1 subset is present mainly at baseline in both groups, while the other subsets arose sequentially from AM1 following infection (Fig. 8A, B). Interestingly, comparison of PLWH + Mtb versus HC + Mtb groups by GSEA across the four AM subsets reveals that deficits in the AM3 subset proinflammatory functions are primarily responsible for the inability to upregulate inflammatory cytokine-mediated signaling pathways in PLWH following Mtb infection. AM3 subsets present in PLWH + Mtb have prominent defects in TNF signaling pathways (Fig. 8C) and have significantly lower expression of key proinflammatory genes (Fig. 8D). Pseudotime analysis comparing TNF signaling cascades across AM1-AM4 subsets in HC + Mtb *versus* PLWH + Mtb shows a striking pattern of AM3 subsets acquiring TNF-TNFR signaling following Mtb infection in HC (Fig. 8E). In contrast, AM3 subsets from PLWH do not acquire these genes upon stimulation with Mtb and show impaired TNF signaling via NFκB. Thus, AM3 subsets from PLWH are significantly impaired in their activation status and capacity to induce TNF and other proinflammatory cytokine responses necessary for controlling Mtb infection. Taken together, these results demonstrate that AMs from PLWH are impaired in their capacity to develop into fully

https://doi.org/10.1038/s41467-025-57668-y

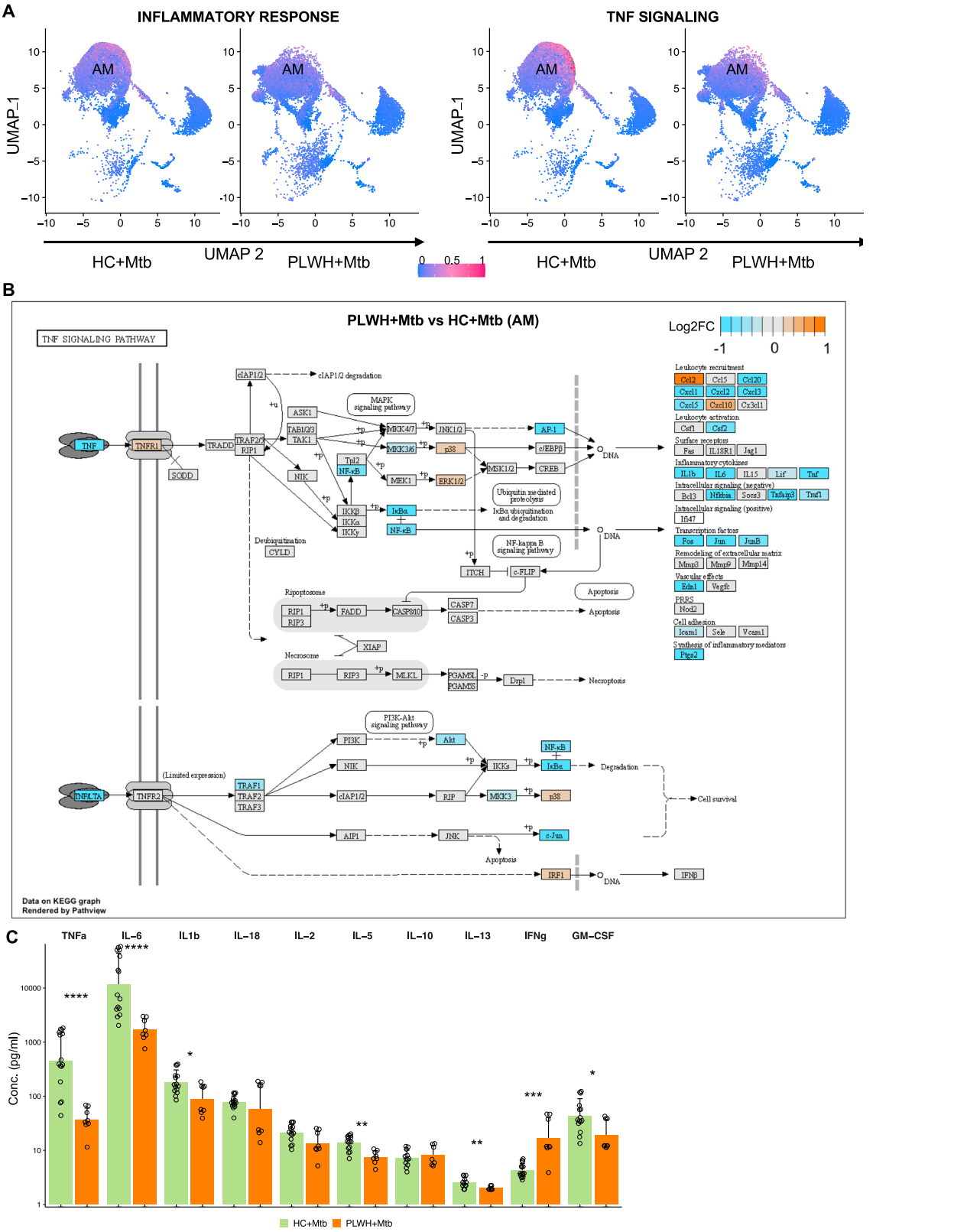

Fig. 6 | Inflammatory responses and TNF signaling in Mtb-infected AMs from PLWH compared to HCs. A UMAP shows the pathway enrichment score for inflammatory pathway (left panel) and TNF signaling pathway (right panel). Pathway enrichment score for each cell ranges from low (blue) to high (pink). **B** Pathway analysis of KEGG TNF signaling pathway using pathview. Genes are colored by log2 fold change between PLWH + Mtb vs HC + Mtb. **C** Concentration of inflammatory cytokines quantified using Luminex technology in HC + Mtb ($n = 6$) and PLWH + Mtb ($n = 3$). *X*-axis shows the various cytokines, and *y*-axis shows the concentration. Each dot represents individual sample, and the bar shows the mean. Data is represented as mean ± SEM. Difference in the means was estimated using two-sided Wilcoxon non-parametric *t*-test. ***, $p < 0.001$; ****, $p < 0.0001$.

https://doi.org/10.1038/s41467-025-57668-y

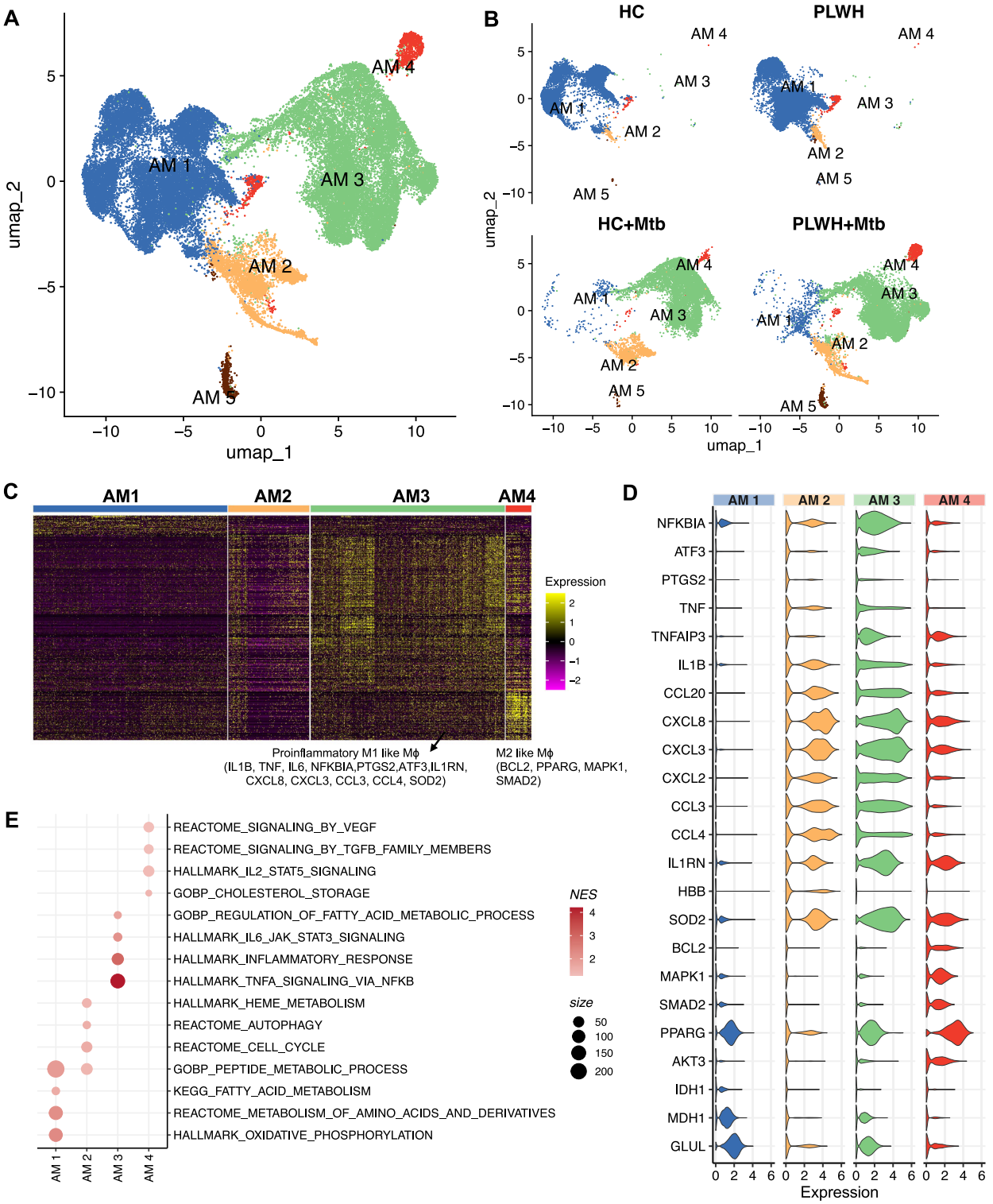

Fig. 7 | Distinct AM subsets in the airways of HC and PLWH with and without Mtb infection. A Concatenated UMAP of HC, PLWH, HC + Mtb, and PLWH + Mtb shows various AM subsets identified using Seurat clusters. **B** UMAP shows AM subsets in HC, PLWH, HC + Mtb, and PLWH + Mtb groups. **C** Transcriptional profile of top genes representative of each cluster is shown as heat map. Normalized expression values are plotted ranging from low (pink) to high expression (yellow). Notable genes from AM3 and AM4 clusters are labeled at the bottom. **D** Violin plot shows the normalized expression of genes representative of each AM subset. **E** Bubble plot shows the significantly enriched pathways each AM subset obtained from gene set enrichment analysis (GSEA) in various T cell subsets. Up-regulated pathways in each AM subset compared to other AM subsets are shown in red, while downregulated pathways are shown in blue. The size of the bubble represents the size of the reference pathway.

https://doi.org/10.1038/s41467-025-57668-y

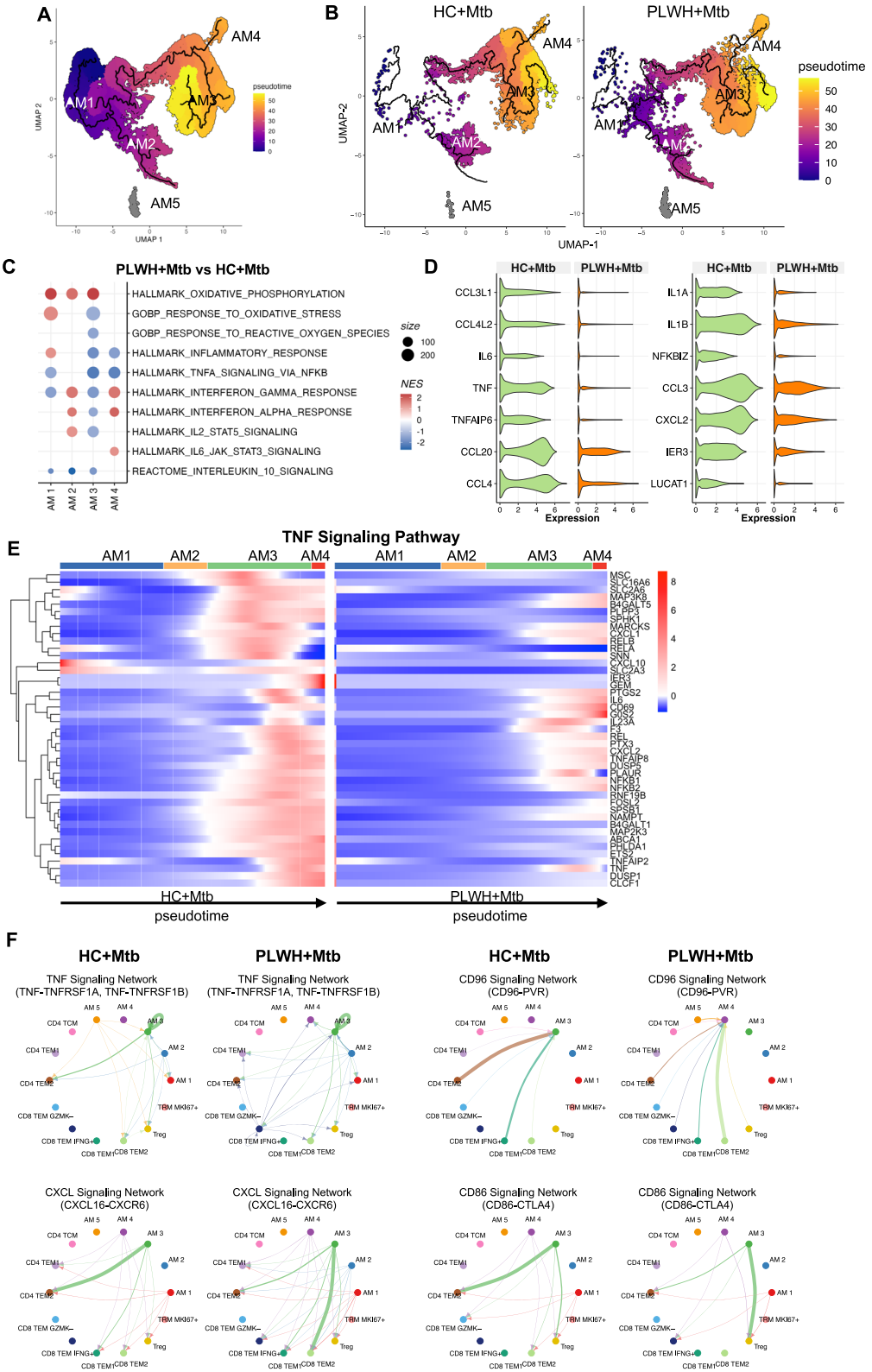

Fig. 8 | TNF signaling networks in AM3 subsets from PLWH in response to Mtb infection. A Concatenated UMAP of HC, PLWH, HC + Mtb, and PLWH + Mtb shows AM subsets color coded by pseudotime. The cells are color-coded from early (violet) to later (yellow) timepoint in pseudotime. **B** UMAP shows the AM subsets in HC + Mtb and PLWH + Mtb colored by pseudotime. **C** Bubble plot shows the enriched pathways between PLWH + Mtb and HC + Mtb in different AM subsets obtained from gene set enrichment analysis (GSEA). Up-regulated pathways are shown in red, while downregulated pathways are shown in blue. The size of the bubble represents the size of the reference pathway. **D** Violin plot shows the distribution of top DEGs in PLWH + Mtb vs HC + Mtb in AM3 subset. **E** Heatmap shows the expression of differentially expressed genes in the TNF signaling pathway across the pseudo-space. Each row shows the gene clustered hierarchically in HC + Mtb and PLWH + Mtb groups. The bar at the top indicates the estimated annotation of cells. **F** Cell-cell communication network shows the putative interactions between ligand and receptor pairs in HC + Mtb and PLWH + Mtb. The arrow indicates the directionality of interaction, and the width of the edge indicates the strength of communication.

activated M1-like proinflammatory effector cells that are necessary for mounting effective immune responses to Mtb.

Defects in crosstalk between M1-like alveolar macrophages and airway T cells in PLWH on ART

We next asked whether cell-cell communication networks between specific AM and T cell subsets were altered in PLWH compared to HC following Mtb infection. CellChat analyzes highlighted key AM-T cell interaction networks that were significantly enriched in HC + Mtb versus PLWH + Mtb. Specific pathways of interest are represented in Fig. 8F, showing crosstalk between AM and T cell subsets within each pathway. Cell-cell communication network analysis shows that the activated M1-like AM3 subset is the major immune cell predicted to engage with T cells *via* TNF-TNFRSF1A/1B, Lck-CD8A/B1, CXCL16-CXCR3, CD86-CTLA4 and PGE2-PTGES interactions (Fig. 8F and Supplementary Fig. 4). The AM3 subset shows strong interactions with CD4 effector memory T cells in HC (CD4 T_{EM2}), in the context of pathways related to proinflammatory responses, T cell activation and immune cell recruitment. However, these interactions are significantly diminished or absent in PLWH, where interactions with chronically immune-activated CD8 T_{EM} subsets and T_{regs} dominate. Moreover, PLWH harbor interactions between anti-inflammatory AM4 and T cells within the CD96-PVR axis, which is involved in promoting immunosuppression in many pathological conditions, such as tumors (Fig. 8F). These results suggest that critical AM interaction networks required for effective immunity against Mtb in lung compartments are absent in PLWH on ART.

Alveolar macrophages from PLWH exhibit an anti-inflammatory and immunosuppressive profile

To validate our bioinformatics predictions at the cellular level, we performed flow cytometry analysis and intracellular cytokine staining on BAL cells after 4 h and 24 h of ex vivo Mtb infection using a panel that included phenotypic and functional macrophage markers. We observed that frequencies of TNF secreting AMs were lower in PLWH compared to HC after 4 h of Mtb infection. Additionally, we found that even after 24 h of Mtb infection, TNF secreting AMs did not recover and continued to remain at relatively low levels in PLWH compared to HC (Fig. 9A, B and Supplementary Fig 5A). Responses to stimulation with TLR ligands were, however, comparable in both groups (Supplementary Fig. 5B–E). The frequencies of IL-6$^+$, HLA-DR$^+$, CD40$^+$ and CD80$^+$ were also observed to be relative lower in PLWH compared to HC at both 4 h and 24 h after Mtb infection, indicating potential impaired activation and costimulatory capacity (Fig. 9B). To further understand differences between the profiles of AMs in HC versus PLWH, we performed high dimensional analysis of the flow cytometry data using a combination of phenotypic and functional markers from all timepoints. TNF, IL-6, CD38, HLA-DR, IL-10, and CD200R were used for dimensionality reduction using UMAP and then clustered using ClusterExplorer. We identified three distinct subsets of AMs consisting of one smaller population, Pop0, and two larger populations, Pop1 and Pop2 (Fig. 9C, E). Pop0 was IL-6$^+$, TNF$^+$ but negative for activation markers CD38 and HLA-DR and negative for IL-10 and the immunosuppressive receptor CD200R. Pop1, annotated as proinflammatory and activated (IL-6$^+$, TNF$^+$, CD38$^+$, HLADR$^+$, IL-10$^+$, CD200R^{low}; Fig. 9D), emerged as the major population in HCs (Fig. 9E, F top panel). Pop2 expressed both the anti-inflammatory cytokine IL-10 and high levels of the immunosuppressive receptor CD200R but was negative for TNF and IL-6 (IL-6^{neg}, TNF^{neg}, CD38$^+$, IL-10$^+$ and CD200R$^+$, Fig. 9D) and was the dominant population in PLWH (Fig. 9E, F). The enrichment of TNF and IL-6 expression in Pop1 from HC versus the enrichment of IL-10 and CD200R in Pop2 from PLWH is further highlighted in Fig. 9F. We next quantified Pop1 and Pop2 subsets in uninfected and Mtb-infected samples from HC and PLWH groups. Fig. 9G, H show that frequencies of IL-10$^+$CD200R$^+$ AMs were significantly higher in PLWH compared to HCs both at baseline and after Mtb infection. Further, we found that TNF^{neg} AMs from PLWH expressed both IL-10 and CD200R, whereas HCs had very low frequencies of TNF^{neg} IL-10$^+$CD200R$^+$ AMs. In contrast, AMs that were positive for TNF$^+$ did not express IL-10 and CD200R.

In summary, our data indicate that PLWH on ART are unable to mount effective TNF-TNFR signaling networks and related proinflammatory responses to Mtb in their airways. Further, we provide evidence for impaired crosstalk between AMs and T cells in PLWH, which together suggest aberrant immunity to Mtb infection in lung compartments. Moreover, the presence of AM subsets expressing IL-10 and CD200R in PLWH following Mtb infection suggest immunoregulatory functions that may suppress proinflammatory responses and hinder effective immunity. Developing therapies that target these deficits has potential to improve outcomes for PLWH on ART. Moreover, our studies provide new insights that may be applicable to other opportunistic respiratory infections that affect PLWH on ART.

Discussion

Although we have known for many years that the risk of chronic lung disease and respiratory infections such as Mtb in people living with HIV (PLWH) remains high despite ART[4,7,23], the lung immune responses that promote susceptibility to TB in PLWH undergoing ART remain unclear. Here, we have used single-cell approaches to comprehensively evaluate immune responses to Mtb in BAL cells from the airways of PLWH and HCs. To our knowledge, this is the first study to assess the single-cell transcriptome of PLWH on ART, thereby expanding our understanding of AMs and their cellular interaction networks in human lung compartments and providing new insights into aberrant immune responses to Mtb in PLWH on ART. Using single cell transcriptomics and high-dimensional flow cytometric data of BAL cells, we showed that AMs constituted most of the BAL cells as expected[24–26], but we also identified neutrophils, eosinophils, monocytes, NK cells, dendritic cells (DCs), CD4/CD8 T cells, γδ T cells, T_{regs}, and epithelial cells (Fig. 1). Notably, we observed high concordance in the identified cell types and their proportions between ScRNAseq and flow cytometry. Our studies identified several differentially expressed genes (DEGs) between HC and PLWH across multiple myeloid and lymphocytic cell types present in BAL, with the most significant transcriptional changes occurring post-Mtb infection (Figs. 2–3). Notably, antigen presenting cells (APCs) from PLWH, such as AMs, DCs and monocytes, had significantly lower expression of multiple genes corresponding to proinflammatory cytokine pathways downstream of TNFSF-TNFRSF signaling: TNF, APRIL, BAFF, IL-6, IL-1 and IFN-γ, compared to HC (Figs. 3, 5–6) but showed comparable responses to stimulation with TLR ligands such as LPS, Pam_3Cys_4 and zymosan (Supplementary Fig. 4). Importantly, AMs were the main drivers of both robust TNF signaling in HCs, as well as of the defects in TNF signaling networks in PLWH on ART.

TNF, a pleiotropic cytokine that is rapidly released by AMs and monocytes after infection or trauma, plays a central role in activating macrophages, recruiting inflammatory immune cells, and orchestrating the induction of pro-inflammatory cascades and antimicrobial activity against pathogens[27,28]. TNF binds to its cognate receptors TNFR1 and TNFR2, resulting in activation of either canonical or non-canonical NFκB signaling pathways, respectively[28,29]. The binding of TNF to TNFR1 triggers TRADD-TRAF2-RIP1 mediated NFκB signaling, leading to upregulation of inflammatory cytokine and chemokine production, lipid mediators, and apoptotic pathways[28,30]. TNF is a critical cytokine for controlling intracellular bacterial infections and synergizes with IFN-γ to enhance killing of Mtb and contain bacteria within organized granulomas[31,32]. Blockade of TNF has been shown to increase susceptibility to Mtb infection by disrupting granuloma structure and promoting dissemination of mycobacteria[33]. Studies using mice with cell-type-specific TNF deficiency showed that TNF from macrophages and neutrophils mediated transient early control of

https://doi.org/10.1038/s41467-025-57668-y

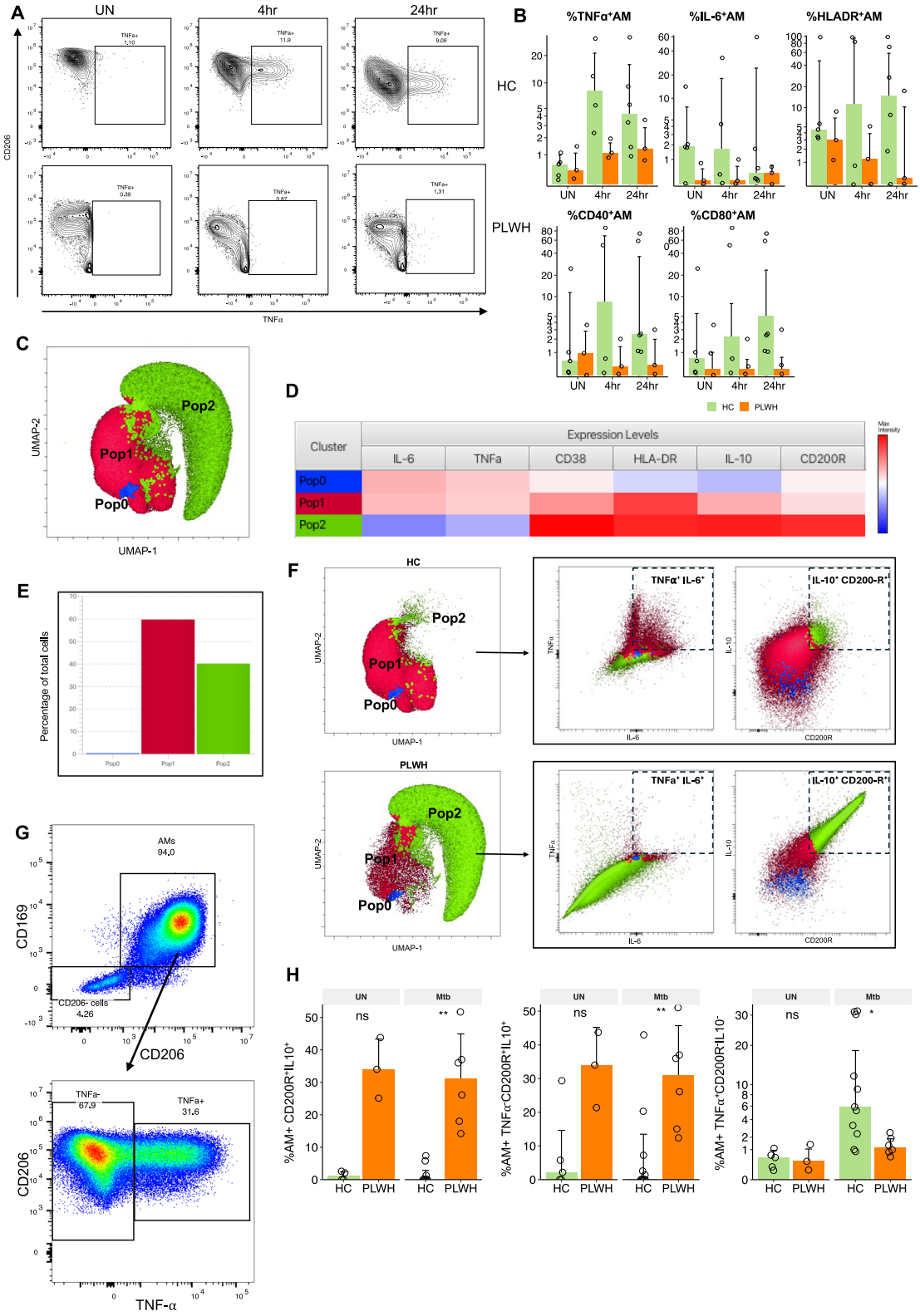

Mtb, while T-cell derived TNF was necessary for sustained protection during chronic Mtb infection[34]. TNF-neutralizing drugs have also been linked to increased rates of latent TB reactivation in humans. Anti-TNF monoclonal antibodies or soluble TNF receptors administered to treat chronic inflammatory diseases, such as rheumatoid arthritis, psoriasis, and inflammatory bowel disease, can increase the relative risk of TB up to 25 times, depending on the clinical setting and the TNF antagonist used; for example, anti-TNF antibodies such as infliximab inhibit T cell functions, and are associated with a higher risk of TB than soluble TNF receptor therapy with etanercept[35,36]. Our data show that PLWH on ART are inherently unable to mount TNF-TNFR1 signaling networks between AMs and T cell subsets in the lung, which suggests that their increased susceptibility to TB in these individuals is in large part due to defects in TNF and downstream proinflammatory functions of AMs. Moreover, our data support the idea that the role of TNF signaling in containing Mtb infection within lung granulomas and preventing

Fig. 9 | High dimensional flow cytometry analysis of AMs in HC and PLWH in response to Mtb infection. A Representative flow cytometry plots show the frequency of TNF^+ AMs in HC and PLWH at baseline and at 4 h and 24 h after infection. **B** Frequency of AMs positive for inflammatory cytokine and activation marker of HC + UN ($n = 5$), PLWH + UN ($n = 4$), HC + Mtb 4 h ($n = 4$), PLWH + Mtb 4 h ($n = 3$), HC + Mtb 24 h ($n = 6$) and PLWH + Mtb 24 h ($n = 3$) are shown. Data is represented as median ± SEM. The difference in the means was calculated using two-sided Wilcoxon non-parametric test. None of the groups showed significant differences. **C** UMAP projection shows the combined events obtained by down sampling to select 12,000 AM events from each sample ($n = 3$ for both HC and PLWH). The clustering was performed using FlowSOM/ClusterExplorer. **D** Heatmap shows the relative MFI of markers used for UMAP and clustering in (**C**). **E** Percentage of each population of the total cells. **F** UMAP of HC and PLWH are shown on the left panel. The right panel shows the visualization 2D plots from the UMAP. The contribution of each cluster for the expression of either TNF/IL-6 or IL-10/CD200R is shown. **G** Gating strategy of $CD200R^+IL10^+$ AMs (top panel), TNF^{neg} $CD200R^+IL10^+$ AMs (bottom panel), and $TNF^+CD200R^{neg}IL10^{neg}$ AMs (bottom panel) in HC and PLWH with and without Mtb infection are shown. **H** Frequency of $CD200R^+IL10^+$ AMs (left panel), TNF^{neg} $CD200R^+IL10^+$ AMs (middle panel), and $TNF^+CD200R^{neg}IL10^{neg}$ AMs (right panel) in HC and PLWH with and without Mtb infection are shown. Uninfected groups are labeled as UN (HC, $n = 6$; PLWH, $n = 3$), and Mtb group includes samples after 4 h or 24 h post-infection (HC, $n = 11$; PLWH, $n = 6$). Data is represented as median ± SEM. Barplot shows the median, and each dot represents individual sample. Statistical difference between UN and Mtb groups was estimated using two-sided Wilcoxon non-parametric test. *, $p < 0.05$; **, $p < 0.01$; ns, not significant.

dissemination, as seen in animal models, is likely also in play in humans. Indeed, we know that increased rates of disseminated, extrapulmonary TB are more common in PLWH compared to people without HIV[37]. A recent study reported on two patients with inherited TNF deficiency who presented with recurrent TB even after previous anti-TB treatment. Alveolar macrophage-like cells derived from these patients and subsequently infected with Mtb in the presence of exogenous TNF showed reduced bacterial burden and increased oxidative burst compared to cells lacking TNF[38]. These results suggest that provision of exogenous TNF to AMs from PLWH on ART may have the capacity to restore their antimicrobial functions. Our future studies will explore the impact of exogenous TNF on AM responses to Mtb in PLWH.

Another recent study reported alterations in TNF signaling in transcriptionally profiled monocytes obtained from HC and PLWH, who were either latently infected with Mtb (LTBI) or classified as resistors (RSTR): i.e., individuals who were highly exposed to TB cases but who did not test positive by interferon gamma release assay (IGRA). Monocytes from the RSTR group had significantly higher TNF signaling and inflammatory responses to in vitro infection with Mtb compared to LTBI in HIV-uninfected persons. However, in PLWH, TNF responses were dampened, with no significant differences between RSTR and LTBI arms[39]. Notably, in our study, we observed significantly lower TNF signaling in monocytes within BAL cells from PLWH on ART infected with Mtb compared to HC; however, the relatively low proportions of these cells precluded further study. AMs are the major subset in BAL and are the first cells to encounter Mtb. Macrophages from ART naïve PLWH have been shown to elicit impaired phagocytic function[40]. However, contrasting results have been observed too[41], and detailed understanding of effect of Mtb in AMs from PLWH is lacking. While the basis for defective TNF-TNFR signaling in PLWH on ART remains unclear, a recent study of BAL from PLWH, HC, and individuals on PrEP reported that AMs from PLWH on ART had weaker TNF expression and epigenetic impairments following Mtb infection compared to HC[22]. Specifically, they noted greater chromatin accessibility and histone acetylation in chromatin regions corresponding to TNF, IFN, and NFkB signaling, suggesting that defects in TNF signaling may be due to epigenetic alterations at TNF and other proinflammatory loci within AMs from PLWH on ART[22]. We know that histone acetylation is catalyzed by histone acetyltransferases that transfer the acetyl group from acetyl-CoA to the ε-amino group of lysine residues, producing coenzyme A. Thus, production of acetyl-coA is central to carbon metabolism within cells, connecting catabolism, anabolism, and energy generation[42]. In mitochondria, acetyl-CoA is a product of catabolism either from glycolysis-generated pyruvate, fatty acid β-oxidation (FAO), or amino acid degradation[43]. Our scRNAseq analyzes show that Mtb-infected AMs from PLWH show higher levels of mitochondrial OXPHOS compared to HC, indicating a metabolic imbalance consistent with lower glycolysis and FAO. Since macrophages are known to upregulate glycolysis and downregulate OXPHOS upon infection with Mtb[44,45], our data suggest that AMs from PLWH on ART are unable to mount adequate metabolic responses to energy-intensive activities such as Mtb infection. We know that upregulation of glycolytic metabolism in M1-like proinflammatory macrophages leads to production of antimicrobial effectors such as iNOS and Th_1 responses, while alternatively activated M2-like macrophages have higher levels of OXPHOS, which promotes anti-inflammatory functions[44]. TNF can also mediate control of Mtb infection via induction of mitochondrial reactive oxygen species (ROS) through RIP1-RIP3-dependent pathways[46], as reflected by the reduced response to oxidative stress and ROS in AM3 subsets from PLWH on ART. We speculate that dysregulation of the balance between pro-and anti-inflammatory AM immunometabolism in response to Mtb in PLWH leads to suboptimal AM-T cell crosstalk and ineffective T cell functions. While the links between metabolic state and immune function of macrophages are increasingly appreciated, very little is known about how the metabolic state of human AMs influences their effector functions in response to Mtb in HC versus PLWH. Thus, our data warrant future studies focused on delineating the relationships between AM metabolism and their immune effector functions to understand the mechanisms underlying the TNF signaling defects in PLWH on ART. Interestingly, glyceraldehyde 3-phosphate dehydrogenase (GAPDH), a key enzyme in the glycolytic pathway, has been shown to regulate TNF secretion. When glycolysis is limited, GAPDH binds to TNF mRNA and limits its translation[47]. PLWH on ART have been reported to exhibit lower oxygen consumption rates and mitochondrial bioenergetics compared to HC[48], consistent with lower glycolytic metabolism. In future studies, we will investigate the links between immunometabolism and chromatin accessibility in AMs at baseline and after Mtb infection and delineate how they influence TNF transcription, secretion, and downstream signaling pathways.

TNF signaling is also known to promote macrophage differentiation[29]. Thus, the rapid generation of the M1-like AM3 subset in HC following Mtb infection (Fig. 7), and the failure to acquire expression of genes associated with full activation and TNF-TNFR signaling in AMs from PLWH (Fig. 8) suggests that the capacity to differentiate into potent proinflammatory and antimicrobial AMs, rather than the numbers of AMs present in lungs of PLWH, drives the eventual control or expansion of Mtb. Additionally, the pattern of chemokine expression in AM3 subsets (Fig. 7) characterizes them as bona fide sentinel cells that produce chemoattractants such as Cxcl2 (MIP2α), Cxcl3 (MIP2β), Cxcl5, and Cxcl8, which promote neutrophil migration to the site of infection. Ccl20 and Cxcl16 are strongly chemotactic for T cells via binding to CCR6 and CXCR3, respectively, thus facilitating antigen presentation and generation of effector Th_1 and cytotoxic CD8 T cells and memory T cells[49]. The TNFSF member APRIL is also produced by AMs and monocytes and promotes the expression of proinflammatory mediators such as Cxcl8 and metalloprotease 9 (MMP-9) upon binding to its receptors TACI and BCMA[50]. Overall, the aberrant differentiation trajectory of AMs in PLWH + ART, along with diminished AM3-CD4 T cell interactions within TNF-TNFR1 and costimulatory networks, demonstrates defective activation and

differentiation of AMs in the lung compartments of PLWH. Interestingly, we identified a distinct AM4 subset that was enriched in PLWH following Mtb infection. AM4 subsets harbored TGF-β signaling and cholesterol storage pathways but downregulated TNF and other inflammatory pathways upon Mtb infection, indicating an M2-like profile with low proinflammatory capacity. Moreover, cell-cell communication analysis highlighted that AM3 subsets from PLWH were predicted to preferentially interact with T_{regs} or CD8 T cells rather than CD4 effector T cells. TGF-β has been shown to be critical in maintaining immune cells in a resting state by inhibiting cell activation, and resting cells are the main cellular reservoir for HIV in persons on long-term ART. TGF-β signaling has been implicated in promoting HIV latency in the airways of PLWH on ART[51], and increasing HIV viral reservoir load could further exacerbate HIV-associated lung coinfections such as Mtb. Higher frequencies of provirus have also been seen in T_{regs} relative to effector CD4 T cells, and T_{regs} can inhibit cell-mediated immunity through immunosuppressive mechanisms[52]. However, the role of T_{regs} in the airways of PLWH on ART remains unclear. Additionally, interactions between AM4 subsets and CD8 T cells within immunosuppressive signaling networks such as PVR-CD96, as well as increased CD39 and LIGHT signaling between AMs and T cells, were predicted to occur in PLWH post-Mtb but not in HC. Additional research is needed to delineate potential links between TGF-β signaling, immunometabolism, and the induction of T_{regs} and other immunosuppressive pathways in the lungs of PLWH.

Validation of our scRNAseq results by flow cytometry further supports the idea that AMs from HCs and PLWH diverge in their functional responses to Mtb (Fig. 9). TNF and IL-6 secreting AMs were significantly reduced in PLWH compared to HC along with expression of other activation and costimulatory markers such as HLA-DR, CD40 and CD80 (Fig. 9). These data mirror the M1-like AM3 subset that was reduced in PLWH compared to HC (Figs. 4–5). Moreover, high dimensional analysis allowed us to identify a subset of AMs enriched in PLWH that displayed features of M2-like macrophages, with high expression of IL-10 and the immunosuppressive receptor CD200R, along with the absence of TNF and IL-6 expression (Fig. 9). CD200R is an immunoglobulin superfamily member that was first identified as an orexin receptor type 2 and is largely restricted to myeloid cells[53,54]. Interaction between CD200R and its ligand CD200 results in attenuation of proinflammatory responses in diverse disease states, including autoimmunity and cancer[55–58]. In the lung, CD200R engagement has been shown to inhibit effector functions and reduce inflammation during asthma, indicating an immunoregulatory role for CD200R[59]. In macrophages, CD200R engagement inhibited IFN-γ and IL-17 mediated IL-6 and TNF secretion in macrophages, and alternatively activated M2 macrophages were reported to express CD200R[54,60]. Leishmania infection of macrophages in vitro was shown to increase CD200R and IL-10, while blocking CD200-CD200R interaction resulted in decreased parasite burden and enhanced macrophage activation and Th_1 polarization[61]. Thus, upregulation of CD200R and IL-10 in Mtb-infected AMs from PLWH reported here (Fig. 9) along with the predicted enrichment of M2-like AM4 subsets and increased IL4/IL13/IL-10 signaling (Figs. 7, 8), suggest that manipulating the CD200-CD200R axis will provide further insights into the potential immunosuppressive role of this pathway. Overall, our data support a model in which AMs from PLWH are unable to effectively recruit inflammatory cells to the lung and mount antimycobacterial defenses but rather promote immunosuppression and dysfunctional T cell responses that fail to protect against progression to TB disease.

The wide range T cell subsets in the airways identified by our scRNAseq analyzes, and the altered AM-T cell interaction networks inferred from CellChat analyzes, provide important new insights into the lung environment in otherwise healthy persons with and without HIV. Effector memory CD4 T cells expressing IFN-γ and TNF ($CD4T_{EM2}$) and CD8 T cells ($CD8T_{EM1}$) expressing cytotoxic molecules such as granzyme B, perforin and granulysin were detected in the airways of HC (Fig. 4) but were almost absent in PLWH, suggesting that effector T cell responses to Mtb infection are likely to be sub-optimal in PLWH on ART. Moreover, CellChat networks show M1-like proinflammatory AM1 -effector memory T cell interactions in HC (i.e., TNFSF-TNFRSF, CXCL16-CXCR3, CD86-CTLA4, PGE2-PGES3/R4), pointing to robust T cell activation, co-stimulation, and effector functional capacities. On the other hand, PLWH harbored CD8 T cell subsets ($CD8T_{EM2}$) that had a hyper-activated phenotype with higher IL-4/IL-13 and IL-10 signaling, and T_{regs} that upregulated IL-10 were also present at significantly higher levels in PLWH compared to HC. These data are consistent with the chronic immune activation and residual inflammation reported in PLWH on ART[19,62,63], including after controlling for age and HIV related factors such as lower CD4 T cell counts[64,65]. While our data do not distinguish between bystander versus antigen-specific T cell phenotypes due to the low T cell frequencies and the short duration of ex vivo infection, we anticipate that future research focused on understanding the lung environment in PLWH with latent or active TB, particularly in areas where these two pandemics are endemic, will be fruitful.

Our data extend and support published studies that have characterized the landscape of human BAL cells from persons with latent Mtb infection (LTBI) and ART-naïve PLWH with active TB[26]. AMs from ART-naïve PLWH were impaired in phagocytosis of reporter beads[40], while another study reported normal internalization and killing of *Salmonella typhimurium*[41]. ART-naïve PLWH also showed lower TNF release and AM apoptosis compared to HCs[66]. A recent study compared the BAL single cell landscape in ART-naïve PLWH with or without TB and found that TB led to enrichment of pathways corresponding to antiviral responses such as to type I interferon, while PLWH without TB were enriched for pathways involved in humoral responses and antigen presentation[26]. A type I interferon signature was also observed in the peripheral blood of ART-naïve PLWH at baseline but was absent in BAL[67], highlighting compartmentalization of immune responses that are likely retained even after ART.

A significant strength of our study is the successful comprehensive immunophenotyping and transcriptional profiling of BAL cells at single-cell resolution from the airways of persons with and without HIV. However, the relatively low number of individuals within each group and the inclusion of smokers in both groups are limitations. Our study also has some other limitations. We recognize that we were not able to distinguish between the relative contributions of the ART regimen itself and chronic HIV infection as we did not directly examine the effect of ART on the transcriptional response to Mtb in HIV-uninfected persons at the single-cell level. The recent study by Correa-Macedo et al. used ATAC-seq approaches to show that AMs from PLWH on ART had impaired epigenetic responses after 18 h of ex vivo Mtb infection compared to healthy HIV-uninfected controls[22]. Interestingly, they also observed some of these changes in individuals receiving ART regimens as preexposure prophylaxis (PrEP), suggesting that in addition to HIV infection, ART regimens may impact AM responses to Mtb. Extending the insights generated from our current single-cell studies of the BAL cells to examining responses to Mtb in individuals on PrEP at the single-cell level will provide additional key insights into the relative contributions of HIV infection and ART to immune functions. Rigorously studying the effect of PrEP will involve large cohort sizes and careful selection of participants undergoing similar PrEP regimens that was beyond the scope of our current study. The clinical reality for PLWH is lifelong treatment; thus, delineating the signaling pathways that contribute to increased risk of developing TB in PLWH on ART, as reported here, addresses a critical knowledge gap that could lead to new adjunctive therapies for people living with HIV and TB. Our studies also do not address whether impaired AM functions and dysregulated T cell responses to Mtb in PLWH are directly impacted by the presence of intact or defective virus within lung cells. Previous studies

demonstrated that AMs from the BAL of otherwise healthy PLWH on ART had detectable HIV proviral DNA, and HIV RNA was quantified within AMs in a subset of these individuals even when plasma HIV RNA was undetectable[20]. Further, residual inflammation and higher levels of oxidative stress have been reported in the BAL of PLWH on ART[68]. Assessing the extent to which HIV persistence within AMs and/or CD4 T cells in the lung drives the compromised immune defense pathways described in this study will be an important future direction of research that would not only extend our current findings but open new avenues for therapeutic intervention.

Methods

Study design and participants

This study protocol was reviewed and approved by the Emory University Institutional Review Board (IRB) and the Research & Development Committee of the Atlanta Veterans Administration Medical Center (VAMC). The study participants consisted of persons living without HIV as healthy controls (HC, $n = 9$) and a group of people living with HIV on antiretroviral treatment (ART) (PLWH, $n = 7$). Signed informed consent was obtained from all the participants. Inclusion criteria: age > 21 years, no history of TB disease or treatment, no signs or symptoms of active TB disease, no history of prior latent TB diagnosis, no history of prior latent TB treatment. For PLWH, all participants were stable on ART for greater than or equal to 12 months with a CD4 count greater than or equal to 200 μL (Table 1). Exclusion criteria: obstructive lung disease (FEV1/FVC < 70% of predicted), active liver disease (known cirrhosis and/or direct bilirubin > 2.0 mg/dL), heart disease (ejection fraction < 50%, h/o acute myocardial infarction, New York Heart Association (NYHA) II-IV cardiac symptoms), renal disease (dialysis-dependent or creatinine > 2.0 mg/dL), taking immunosuppressive medications, bleeding disorders such as thrombocytopenia or significant gastrointestinal bleeding within the past year, pregnancy or currently breast-feeding, new or increasing respiratory symptoms, fever within 4 weeks prior to enrollment.

Bronchoalveolar lavage and sample processing

Bronchoscopies were performed after an overnight fast. Participants underwent flexible fiberoptic bronchoscopy with standardized bronchoalveolar lavage (BAL) performed using standard conscious sedation techniques as previously described[69]. Approximately 180–210 mL lavage was collected in the right middle lobe of the lung in 30cc aliquots. Collected BAL fluid samples were transported on ice to the Emory Vaccine Center laboratories at the Emory National Primate Research Center within 1 h of sample collection. Fresh BAL fluid was filtered through a 70-μm strainer into a 50 ml falcon conical tube (Falcon, catalog no. 352098) to remove any clumped cells and mucus. Pelleted BAL cells were isolated by centrifugation at 524 × *g* (1500 rpm) for 5 min at 40 °C, and the supernatant was removed and stored. BAL cells were washed twice in 1× DPBS (Gibco, catalog no.14190-144) and resuspended in complete RPMI 1640 media with L-glutamine (Gibco, catalog no. 11875119), 10% fetal bovine serum (Gibco, catalog no. A5669801), and penicillin-streptomycin (Gibco, catalog no. 15140122). Cell counts and viability were determined manually using a hemocytometer under a microscope and trypan blue staining. Cells were incubated for 1 h at 37 °C in a 5% CO_2 incubator and then infected in vitro with freshly prepared H37Rv Mtb.

Preparation of Mtb cultures for infection

Live Mtb experiments were conducted under BSL-3 laboratory conditions. Mtb strains H37Rv were used as previously described[70–72]. Briefly, Mtb strains were grown in liquid media Middlebrook 7H9 (BD Difco, catalog no. 271310) supplemented with 0.5% glycerol (Sigma, catalog no. G6279-1L), 10% oleic acid-albumin-dextrose-catalase (OADC) (BD, catalog no. 212351) and 0.05% Tween 80 (VWR, catalog no. 76348-480) at 37 °C. The Mtb H37Rv stocks were thawed at room temperature in the biosafety cabinet, and the inoculum was washed once with 7H9 media (BD Difco) by centrifugation at 4000 × *g* for 10 min at 23 °C. The supernatant was discarded, and the pellet was re-suspended in 7H9 media and inoculum solution transferred to a 30 ml inkwell. For uninfected controls, only 7H9 media was added to inkwell, and both inkwells were secured into a container and placed onto a 37 °C shaking incubator at 75–100 rpm for 4h until infection time. The Mtb culture was removed from the shaking incubator, transferred to a 50 ml conical tube, and sonicated twice. Cell density OD readings were measured at 600 nm. The volume of the culture required for infection was transferred to a falcon conical tube and centrifuged at 4000 × *g* for 10 min at 23 °C. Following centrifugation, the supernatant was discarded, and the Mtb pellet was re-suspended in complete RPMI1640 media.

Mtb infection of BAL cells

BAL cells were suspended in complete media and seeded in 12-well tissue culture plates (1×10^6 cells per well) and rested for 1 h at 37 °C in a 5% CO_2 incubator before infection. Cells were removed from the incubator and centrifuged at 524 × *g* (1500 rpm) for 5 min at 23 °C. The supernatant was carefully removed by pipetting, leaving cells in 100 μl volume. BLCs were infected with Mtb H37Rv at an MOI of 2:1 (bacteria: cells), and only media was added to control wells. For optimal contact, the cells in the plate were further centrifuged at 524 × *g* (1500 rpm) for 5 min at 23 °C and placed at 37 °C in a 5% CO_2 incubator for 4 h, after which they were centrifuged at 524xg (1500 rpm) for 5 min at 23 °C. Then cells were washed with once with 1× DPBS (Sigma, catalog no D8537-500 mL) and resuspended in complete media.

Bacterial burden enumeration

Mtb-infected BAL cells (4-h infection) in complete RPMI1640 media were centrifuged at 524 × *g* (1500 rpm) for 5 min at 23 °C. Following centrifugation, pelleted cells were re-suspended in Triton X100-Tween-80 and diluted in Triton X100 (Sigma, catalog no. T8787-100ML). BAL cells were then plated on 7H10 Middlebrook agar plates (BD, catalog no. 262710) and incubated at 37 °C for 3 weeks before enumeration of CFU.

Intracellular cytokine staining and flow cytometry

Two hours after Mtb infection, brefeldin A (BFA) (0.5 μg/mL; Sigma, catalog no. B7651-5MG) was added to the wells per manufacturer's instructions. Multiparametric flow cytometry was performed on BAL cells at 0 h and after 4h of Mtb infection (4 h). Single suspensions of BAL cells were stained with live/dead fixable Near-IR surface stain on APC-Cy7 (Invitrogen, catalog no. L10119, 1:2000). Two different flow panels were used. The first panel for immunophenotyping surface proteins using the following antibodies: anti-CD4-BUV 395 (BD 564107 clone L200, 1:100), anti-CD8-BUV496 (BD 612943 clone RPAT8, 1:100), anti-CD169-BUV563 (BD 748926 clone 7-239, 1:100), anti-CD123-BUV661(BD 741541 clone 7G3, 1:200), anti-CD20-BUV737 (BD612849 clone 2H7, 1:100), anti-CD45-BUV805 (BD 612891 clone H130, 1:200), anti-CD206-BV421 (BD 564062 clone 19.2, 1:100), anti-CD24-BV480 (BD 746278 clone ML5, 1:200), anti-CD14-BV605 (BD 564054 clone M5E2, 1:100), anti-HLA-DR-BV650 (BD 564231 clone G46.6, 1:100), anti-CD16-BV711 (BD563127 clone 3G8, 1:200), anti-CD163-BV750 (BD 747185 clone GH/161, 1:100), anti-CD3-BV786 (BD 563800 clone SK7, 1:100), anti-CD71-BB515 (Biolegend 334104 clone CY1G4, 1:50), anti-CD56-BB700 (BD 745894 clone NCAM16, 1:200), anti-CD33-PE (Miltenyi clone AC104.3E, 1:200), anti-CD11b-PE-TR (Dazzle 594) (BD 562399 clone ICRF44, 1:200), anti-CD11c-PE-Cy7 (Biolegend 301608 clone 3.9, 1:200), anti-CD66abce-APC (Miltenyi clone TET2, 1:100), and anti-CD326-Alexa700/R718 (BD 751942 clone EBA-1, 1:50). The second panel for functional assessments used the following antibodies: CD45 on BUV805 (BD 742005 clone D058-1283, 1:200), anti-CD4-BUV395 (BD 564107 clone L200, 1:100), anti-CD8-BUV496 (BD 612943 clone RPAT8,

1:100), anti-CD169-BUV563 (BD 748926 clone 7-239, 1:100), anti-CD40-BUV661 (BD 741624 clone 5C3, 1:200), anti-CD80-BUV737 (BD 741865 clone L307.4, 1:100), anti-CD206-BV421 (BD 564062 clone 19.2, 1:100), anti-PD-1-BV480 (BD 566112 clone EH12, 1:200), anti-CD14-BV605 (BD 564054 clone M5E2, 1:100), anti-HLA-DR-BV650 (BD 564231 clone G46.6, 1:100), anti-CD163-BV750 (BD 747185 clone GH/161, 1:100), anti-CD3-BV786 (BD 563800 clone SK7, 1:100), anti-CD38-FITC (Beckman Coulter IM0775U clone T16, 1:50), anti-CD86-BB700 (BD 566473 clone FUN-1, 1:200), anti-PD-L1-PE (BD 557924 clone MIH1, 1:200), anti-CD11b-PE-TR (Dazzle 594) (BD 562399 clone ICRF44, 1:200) and anti-CD200R-PE-Cy7 (Biolegend 329312 clone OX-18, 1:200). Surface-stained BAL cells were then fixed and permeabilized using the BD kit reagents (catalog no. 555028). Following permeabilization cells were stained against intracellular proteins using the following antibodies: anti-TNF-Alexa700/R718 (BD 566957 clone Mab11, 1:100), anti-IL-6-APC (BD 561441 clone MQ2-13A5, 1:100), and Anti-IL-10-BV711 (BD 564050 clone JES3-9D7, 1:200). Cells were washed after intracellular staining and left in FACS buffer until acquisition on a BD FACSymphony flow cytometer. The analysis was performed using FlowJo (v10.6.1) software[73].

High-dimensional flow cytometry analysis

Manual gating was performed to identify AMs ($CD45^+CD206^+CD169^+$) from both healthy and PLWH samples before and after ex vivo Mtb infection. Flowjo Downsample plugin v3.3.1[74] was used to concatenate equal number of AM events from each sample for further high-dimensional analysis (12,000 events per sample). Using Flowjo plugins, UMAP projection was generated using default parameters and subsequently overlaid with FlowSOM populations to identify the 3 clusters phenotype. Further identification of each sample's clusters and 2D plots was based on the ClusterExplorer[74] visualization plugins. The annotation was based on the combination of fluorophore parameters and heatmap produced by ClusterExplorer.

Cytokine analysis

BAL cells were infected with H37Rv at MOI of 2. After 4 h post infection, BAL cells supernatant was collected and filtered through 0.2 µM syringe filter (CellTreat, catalog no. 229746) into a new tube. Filtered supernatants were transferred out of BSL3 to the lab. Cytokines were measured using the manufacturer's recommended protocol from ProcartaPlex Multiplex Immunoassay (Invitrogen, catalog no. EPX180-12165-901), and data was acquired on MAGPIX, Luminex system.

Bacterial burden enumeration

Mtb-infected BAL cells (4-h infection) in complete RPMI1640 media were centrifuged at 524 × *g* (1500 rpm) for 5 min at 23 °C. Following centrifugation, pelleted cells were re-suspended in Triton X100-Tween-80 and diluted in Triton X100. BAL cells were then plated on 7H10 Middlebrook agar plates (BD, catalog no. 262710) and incubated at 37 °C for 3 weeks before enumeration of CFU.

10X genomics 5′ ScRNAseq chromium capture

After infection, cells were centrifuged and resuspended in incomplete RPMI media at a concentration of ~1×10^6 /ml. Cell counts were performed using Countess slides with viability assessed via trypan blue exclusion prior to capture. Single cell suspensions were prepared and loaded onto the 10X Genomics Chromium Controller in the BSL3 facility using the Chromium NextGEM Single Cell 5′ Library & Gel Bead Kit v1.1 (10x Genomics, catalog no. PN-1000165) to capture individual cells and barcoded gel beads within droplets for reverse transcription. The libraries were prepared according to manufacturer instructions and sequenced on an Illumina NovaSeq 6000 with a paired-end 26 × 91 configuration targeting a depth of 50,000 reads per cell. Cell Ranger software[75] was used to perform demultiplexing of cellular transcript data and mapping and annotation of UMIs and transcripts for downstream data analysis.

ScRNAseq analysis

Raw data was processed with Cell Ranger v6.1.0 (10x Genomics) using standard pipeline. The downstream analysis was performed in R package Seurat v4.3.0[76]. The following criteria were used to filter out cells: nFeatures > 200 and <4500, mitochondrial genes <10%, HBB genes <10%, and ribosomal genes <10%. DoubletFinder v2.0.3[77] was used to identify and filter doublets using default parameters. All the samples at 0 h and 4 h timepoints were integrated using Seurat integration pipeline using default parameters. SCTransform method was used for normalization. The first 15 PC dimensions were used to run UMAP and FindNeighbors functions. The clusters were identified using the FindCluster function with 0.5 resolution.

Major cell types were annotated using SingleR v1.10.0. Human Primary Cell Atlas Data from Celldex v1.6.0 was used as ref. 78. Canonical markers for each cell type were used to verify SingleR cell annotation. These include MARCO, CD68, FCGR3A for AMs, CD68, CD14 and ITGAM for MDMs, S100A8 and S100A9 for neutrophils, CD1C and CD207 for DCs, LYZ for monocytes, CD3E and CD4 for CD4 T cells, CD3E and CD8A for CD8 T cells, CD3D and CD3G for gamma delta T cells, FOXP3 for regulatory T cells, MS4A1 (CD20) and CD79A for B cells, GNLY and PRF1 for NK cells and MUC5AC for epithelial cells. For annotation of AM subsets, AMs were extracted from total cells and re-clustered using the FindCluster function with 0.5 resolution. The top 20 markers from each cluster were used to classify the AM subclusters. T cell subset annotation was performed in an integrated manner. After extraction of T cell from the total cells, cells were re-clustered using resolution of 0.5. Each cluster was then annotated independently by SingleR using two datasets, Encode and Monaco from Celldex as reference[78,79]. Further, marker-based annotation was performed from previously published lung single cell landscape data[80]. Cell annotation was finalized by concordant results from 2 out of 3 cell annotations.

Differential gene expression analysis was performed using FindAllMarkers function using MAST v1.22.0 algorithm[81]. Genes with log fold change greater than 1.3 and adjusted *p* value less than 0.05 were considered up-regulated, and genes with log fold lower than −1.3 and adjusted *p* value less than 0.05 were considered down-regulated genes. The heat map was generated using Heatmap function from ComplexHeatmap package v2.18.0[82]. Venn diagrams were plotted using ggVennDiagram package v1.5.0[83]. Gene set enrichment analysis for each annotated cell population was performed on ranked list of all genes using fgsea v1.22.0[84]. Mapping of gene fold changes to KEGG oxidative phosphorylation pathway was done using pathview v1.36.1[85] using default parameters. Ligand-receptor cell-cell communication prediction between cell populations was done using CellChat v1.5.0[86] using default parameters.

Single cell pathway scoring

R package SiPSiC v1.2.2[87] was used to calculate per-cell pathway scores for pathways of interest. The pathway score is calculated using getPathwayScores function using default parameters.

Trajectory analysis

Trajectories for T cell subsets were constructed using R package Monocle3 v1.3.4[88] using default parameters. Briefly, cells were ordered by assigning CD4 T_{CM} cells as the root node. Trajectories for AM subsets were constructed using R package Slingshot v2.10.0[89] to enable downstream differential expression analysis using R package tradeSeq v1.16.0[90]. Pseudotime analysis was performed by ordering the cells and assigning resting macrophage cluster AM1 as the root node. Differential gene expression analysis along the pseudotime trajectory was done using TradeSeq function fitGAM.

Statistical analysis
All statistical analysis was performed using R v4.2.1[91] and GraphPad Prism v10.1.0[92]. The difference in means between the two groups was calculated using Welch's *t*-test. For differential gene expression analysis and GSEA, adjusted p-values obtained from MAST and fgsea, respectively, were used.

Reporting summary
Further information on research design is available in the Nature Portfolio Reporting Summary linked to this article.

Data availability
Raw and processed data files are available on GEO under accession number GSE266696. All the data used to generate figures are provided via the GitHub repository described in "Code availability." All data are included in the Supplementary Information or available from the authors, as are unique reagents used in this article. The raw numbers for charts and graphs are available in the Source Data file whenever possible. Source data are provided with this paper.

Code availability
All the scripts used in the analysis and to generate figures are available at https://github.com/prashantbajpai/Human_BAL_10x_analysis. All the script can also be accessed from Zenedo using https://doi.org/10.5281/zenodo.14735755.

References

1. Global tuberculosis report 2023. Geneva: World Health Organization; 2023. Licence: CC BY-NC-SA 3.0 IGO. https://www.who.int/teams/global-tuberculosis-programme/tb-reports/global-tuberculosis-report-2023 (2023).
2. Goletti, D., Pisapia, R., Fusco, F. M., Aiello, A. & Van Crevel, R. Epidemiology, pathogenesis, clinical presentation and management of TB in patients with HIV and diabetes. *Int. J. Tuberc. Lung Dis.* **27**, 284–290 (2023).
3. Global tuberculosis report 2020. Geneva: World Health Organization. Licence: CC BY-NC-SA 3.0 IGO. https://www.who.int/publications/i/item/9789240013131 (2020).
4. Alexandrova, Y., Costiniuk, C. T. & Jenabian, M.-A. Pulmonary Immune Dysregulation and Viral Persistence During HIV Infection. *Front. Immunol.* **12**, https://doi.org/10.3389/fimmu.2021.808722 (2022).
5. Trickey, A. et al. Life expectancy after 2015 of adults with HIV on long-term antiretroviral therapy in Europe and North America: a collaborative analysis of cohort studies. *Lancet HIV* **10**, e295–e307 (2023).
6. Trickey, A. et al. Survival of HIV-positive patients starting antiretroviral therapy between 1996 and 2013: a collaborative analysis of cohort studies. *Lancet HIV* **4**, e349–e356 (2017).
7. Gupta, A., Wood, R., Kaplan, R., Bekker, L.-G. & Lawn, S. D. Tuberculosis incidence rates during 8 years of follow-up of an antiretroviral treatment cohort in South Africa: comparison with rates in the community. *PLoS ONE* **7**, e34156 (2012).
8. Hussell, T. & Bell, T. J. Alveolar macrophages: plasticity in a tissue-specific context. *Nat. Rev. Immunol.* **14**, 81–93 (2014).
9. Bissonnette, E. Y., Lauzon-Joset, J.-F., Debley, J. S. & Ziegler, S. F. Cross-talk between alveolar macrophages and lung epithelial cells is essential to maintain lung homeostasis. *Front. Immunol.* **11**, https://doi.org/10.3389/fimmu.2020.583042 (2020).
10. Leiva-Juárez, M. M., Kolls, J. K. & Evans, S. E. Lung epithelial cells: therapeutically inducible effectors of antimicrobial defense. *Mucosal Immunol.* **11**, 21–34 (2018).
11. Ogger, P. P. & Byrne, A. J. Macrophage metabolic reprogramming during chronic lung disease. *Mucosal Immunol.* **14**, 282–295 (2021).
12. Cohen, S. B. et al. Alveolar macrophages provide an early mycobacterium tuberculosis niche and initiate dissemination. *Cell Host Microbe* **24**, 439–446.e434 (2018).
13. Srivastava, S., Ernst, J. D. & Desvignes, L. Beyond macrophages: the diversity of mononuclear cells in tuberculosis. *Immunol. Rev.* **262**, 179–192 (2014).
14. Philips, J. A. & Ernst, J. D. Tuberculosis pathogenesis and immunity. *Annu. Rev. Pathol. Mechanisms Dis.* **7**, 353–384 (2012).
15. Chandra, P., Grigsby, S. J. & Philips, J. A. Immune evasion and provocation by Mycobacterium tuberculosis. *Nat. Rev. Microbiol.* **20**, 750–766 (2022).
16. Gray, J. I. & Farber, D. L. Tissue-resident immune cells in humans. *Annu. Rev. Immunol.* **40**, 195–220 (2022).
17. Deeks, S. G. HIV infection, inflammation, immunosenescence, and aging. *Annu. Rev. Med.* **62**, 141–155 (2011).
18. Pasternak, A. O. & Berkhout, B. HIV persistence: silence or resistance? *Curr. Opin. Virol.* **59**, 101301 (2023).
19. Neuhaus, J. et al. Markers of inflammation, coagulation, and renal function are elevated in adults with HIV infection. *J. Infect. Dis.* **201**, 1788–1795 (2010).
20. Cribbs, S. K., Lennox, J., Caliendo, A. M., Brown, L. A. & Guidot, D. M. Healthy HIV-1-infected individuals on highly active antiretroviral therapy harbor HIV-1 in their alveolar macrophages. *AIDS Res. Hum. Retroviruses* **31**, 64–70 (2015).
21. Yeligar, S. M. et al. Dysregulation of alveolar macrophage PPARγ, NADPH oxidases, and TGFβ1in otherwise healthy HIV-infected individuals. *AIDS Res. Hum. Retroviruses* **33**, 1018–1026 (2017).
22. Correa-Macedo, W. et al. Alveolar macrophages from persons living with HIV show impaired epigenetic response to Mycobacterium tuberculosis. *J. Clin. Investig.* **131**, https://doi.org/10.1172/jci148013 (2021).
23. Jambo, K. C. et al. Asymptomatic HIV-infected individuals on antiretroviral therapy exhibit impaired lung CD4+T-cell responses to mycobacteria. *Am. J. Respir. Crit. Care Med.* **190**, 938–947 (2014).
24. Yang, Q. et al. The interaction of macrophages and CD8 T cells in bronchoalveolar lavage fluid is associated with latent tuberculosis infection. *Emerg. Microbes Infect.* **12**, 2239940 (2023).
25. Liao, M. et al. Single-cell landscape of bronchoalveolar immune cells in patients with COVID-19. *Nat. Med.* **26**, 842–844 (2020).
26. Xiao, G. et al. Uncovering the bronchoalveolar single-cell landscape of patients with pulmonary tuberculosis with human immunodeficiency virus type 1 coinfection. *J Infectious Dis.* https://doi.org/10.1093/infdis/jiae042 (2024).
27. Nunes-Alves, C. et al. In search of a new paradigm for protective immunity to TB. *Nat. Rev. Microbiol.* **12**, 289–299 (2014).
28. Parameswaran, N. & Patial, S. Tumor necrosis factor-α signaling in macrophages. *Crit. Rev. Eukaryot. Gene Expr.* **20**, 87–103 (2010).
29. Wajant, H. & Siegmund, D. TNFR1 and TNFR2 in the Control of the Life and Death Balance of Macrophages. *Front. Cell Dev. Biol.* **7**, https://doi.org/10.3389/fcell.2019.00091 (2019).
30. Jackson-Bernitsas, D. G. et al. Evidence that TNF-TNFR1-TRADD-TRAF2-RIP-TAK1-IKK pathway mediates constitutive NF-κB activation and proliferation in human head and neck squamous cell carcinoma. *Oncogene* **26**, 1385–1397 (2007).
31. Weeratunga, P., Moller, D. R. & Ho, L.-P. Immune mechanisms of granuloma formation in sarcoidosis and tuberculosis. *J. Clin Investig.* **134** https://doi.org/10.1172/jci175264 (2024).
32. Cavalcanti, Y. V. N., Brelaz, M. C. A., Lemoine Neves, J. K. D. A., Ferraz, J. C. & Pereira, V. R. A. Role of TNF-alpha, IFN-gamma, and IL-10 in the development of pulmonary tuberculosis. *Pulm. Med.* **2012**, 1–10 (2012).
33. Flynn, J. L. et al. Tumor necrosis factor-α is required in the protective immune response against mycobacterium tuberculosis in mice. *Immunity* **2**, 561–572 (1995).

34. Allie, N. et al. Prominent role for T cell-derived Tumour Necrosis Factor for sustained control of Mycobacterium tuberculosis infection. *Sci. Rep.* **3**, https://doi.org/10.1038/srep01809 (2013).
35. Brassard, P., Kezouh, A. & Suissa, S. Antirheumatic drugs and the risk of tuberculosis. *Clin. Infect. Dis.* **43**, 717–722 (2006).
36. Schutz, C., Meintjes, G., Almajid, F., Wilkinson, R. J. & Pozniak, A. Clinical management of tuberculosis and HIV-1 co-infection. *Eur. Respir. J.* **36**, 1460–1481 (2010).
37. Alemu, A. et al. Incidence and predictors of extrapulmonary tuberculosis among people living with human immunodeficiency virus in addis ababa, ethiopia: a retrospective cohort study. *PLoS ONE* **15**, e0232426 (2020).
38. Arias, A. A. et al. Tuberculosis in otherwise healthy adults with inherited TNF deficiency. *Nature* **633**, 417–425 (2024).
39. Hong, H. et al. Mycobacterium tuberculosis-induced monocyte transcriptional responses associated with resistance to tuberculin skin test/interferon-γ release assay conversion in people with HIV. *AIDS* **37**, 2287–2296 (2023).
40. Jambo, K. C. et al. Small alveolar macrophages are infected preferentially by HIV and exhibit impaired phagocytic function. *Mucosal Immunol.* **7**, 1116–1126 (2014).
41. Gordon, M. A. et al. Primary macrophages from HIV-infected adults show dysregulated cytokine responses to Salmonella but normal internalization and killing. *AIDS* **21**, 2399–2408 (2007).
42. Wang, Q. et al. Acetylation of metabolic enzymes coordinates carbon source utilization and metabolic flux. *Science* **327**, 1004–1007 (2010).
43. Martínez-Reyes, I. & Chandel, N. S. Mitochondrial TCA cycle metabolites control physiology and disease. *Nature Commun.* **11**, https://doi.org/10.1038/s41467-019-13668-3 (2020).
44. Russell, D. G., Huang, L. & Vanderven, B. C. Immunometabolism at the interface between macrophages and pathogens. *Nat. Rev. Immunol.* **19**, 291–304 (2019).
45. Howard, N. C. & Khader, S. A. Immunometabolism during Mycobacterium tuberculosis Infection. *Trends Microbiol.* **28**, 832–850 (2020).
46. Francisco & Ramakrishnan, L. TNF dually mediates resistance and susceptibility to mycobacteria via mitochondrial reactive oxygen species. *Cell* **153**, 521–534 (2013).
47. Millet, P., Vachharajani, V., McPhail, L., Yoza, B. & McCall, C. E. GAPDH binding to TNF-α mRNA contributes to posttranscriptional repression in monocytes: a novel mechanism of communication between inflammation and metabolism. *J. Immunol.* **196**, 2541–2551 (2016).
48. Einsiedel, L. et al. Mitochondrial dysfunction in CD4+lymphocytes from stavudine-treated HIV patients. *Mitochondrion* **10**, 534–539 (2010).
49. Ranasinghe, R. & Eri, R. Pleiotropic immune functions of chemokine receptor 6 in health and disease. *Medicines* **5**, 69 (2018).
50. Lim, S.-G., Suk, K. & Lee, W.-H. Reverse signaling from LIGHT promotes pro-inflammatory responses in the human monocytic leukemia cell line, THP-1. *Cell. Immunol.* **285**, 10–17 (2013).
51. Chinnapaiyan, S. et al. TGF-β1 increases viral burden and promotes HIV-1 latency in primary differentiated human bronchial epithelial cells. *Sci. Rep.* **9**, https://doi.org/10.1038/s41598-019-49056-6 (2019).
52. Jiao, Y.-M. et al. CD4+CD25+CD127 regulatory cells play multiple roles in maintaining HIV-1 p24 production in patients on long-term treatment: HIV-1 p24-producing cells and suppression of anti-HIV immunity. *Int. J. Infect. Dis.* **37**, 42–49 (2015).
53. Wright, G. J. et al. Lymphoid/neuronal cell surface OX2 glycoprotein recognizes a novel receptor on macrophages implicated in the control of their function. *Immunity* **13**, 233–242 (2000).
54. Jenmalm, M. C., Cherwinski, H., Bowman, E. P., Phillips, J. H. & Sedgwick, J. D. Regulation of Myeloid Cell Function through the CD200 Receptor. *J. Immunol.* **176**, 191–199 (2006).
55. Wedig, J. et al. CD200 is overexpressed in the pancreatic tumor microenvironment and predictive of overall survival. *Cancer Immunol. Immunother.* **73**, https://doi.org/10.1007/s00262-024-03678-6 (2024).
56. Nip, C., Wang, L. & Liu, C. CD200/CD200R: bidirectional role in cancer progression and immunotherapy. *Biomedicines* **11**, 3326 (2023).
57. Ponce-De-León, C. et al. Expression of elafin and CD200 as immune checkpoint molecules involved in celiac disease. *Int. J. Mol. Sci.* **25**, 852 (2024).
58. Lin, M. et al. Inflammatory dendritic cells restrain CD11b+CD4+ CTLs via CD200R in human NSCLC. *Cell Rep.* **43**, 113767 (2024).
59. Shafiei-Jahani, P. et al. CD200–CD200R immune checkpoint engagement regulates ILC2 effector function and ameliorates lung inflammation in asthma. *Nature Commun.* **12**, https://doi.org/10.1038/s41467-021-22832-7 (2021).
60. Koning, N. et al. Expression of the inhibitory CD200 receptor is associated with alternative macrophage activation. *J. Innate Immun.* **2**, 195–200 (2010).
61. Rawat, A. K. et al. The CD200-CD200R cross-talk helps Leishmania donovani to down regulate macrophage and CD4+CD44+ T cells effector functions in an NFκB independent manner. *Int. J. Biol. Macromol.* **151**, 394–401 (2020).
62. Cribbs, S. K., Crothers, K. & Morris, A. Pathogenesis of HIV-related lung disease: immunity, infection, and inflammation. *Physiol. Rev.* **100**, 603–632 (2020).
63. Novelli, S. et al. Persistence of monocyte activation under treatment in people followed since acute HIV-1 infection relative to participants at high or low risk of HIV infection. *eBioMedicine* **62**, 103129 (2020).
64. Kuller, L. H. et al. Inflammatory and coagulation biomarkers and mortality in patients with hiv infection. *PLoS Med.* **5**, e203 (2008).
65. Sandler, N. G. et al. Plasma levels of soluble CD14 independently predict mortality in hiv infection. *J. Infect. Dis.* **203**, 780–790 (2011).
66. Patel, N. R. et al. HIV impairs TNF-α mediated macrophage apoptotic response to mycobacterium tuberculosis. *J. Immunol.* **179**, 6973–6980 (2007).
67. Muema, D. M. et al. Contrasting inflammatory signatures in peripheral blood and bronchoalveolar cells reveal compartment-specific effects of HIV infection. *Front. Immunol.* **11**, https://doi.org/10.3389/fimmu.2020.00864 (2020).
68. Staitieh, B. S. et al. HIV-1 decreases Nrf2/ARE activity and phagocytic function in alveolar macrophages. *J. Leukoc. Biol.* **102**, 517–525 (2017).
69. Prebil, S. E. W., Andrews, J., Cribbs, S. K., Martin, G. S. & Esper, A. Safety of research bronchoscopy in critically ill patients. *J. Crit. Care* **29**, 961–964 (2014).
70. Sia, J. K., Bizzell, E., Madan-Lala, R. & Rengarajan, J. Engaging the CD40-CD40L pathway augments T-helper cell responses and improves control of Mycobacterium tuberculosis infection. *PLoS Pathog.* **13**, e1006530 (2017).
71. Enriquez, A. B. et al. Mycobacterium tuberculosis impedes CD40-dependent notch signaling to restrict Th17 polarization during infection. *iScience* **25**, 104305 (2022).
72. Rengarajan, J. et al. Mycobacterium tuberculosis Rv2224c modulates innate immune responses. *Proc. Natl. Acad. Sci. USA* **105**, 264–269 (2008).
73. FlowJo™ Software for Mac Version 10.9.0. Ashland, OR: Becton, Dickinson and Company; (2023).
74. Quintelier, K. et al. Analyzing high-dimensional cytometry data using FlowSOM. *Nat. Protoc.* **16**, 3775–3801 (2021).
75. Zheng, G. X. Y. et al. Massively parallel digital transcriptional profiling of single cells. *Nat. Commun.* **8**, 14049 (2017).
76. Hao, Y. et al. Dictionary learning for integrative, multimodal and scalable single-cell analysis. *Nat. Biotechnol.* **42**, 293–304 (2024).

77. McGinnis, C. S., Murrow, L. M. & Gartner, Z. J. DoubletFinder: doublet detection in single-cell RNA sequencing data using artificial nearest neighbors. *Cell Syst.* **8**, 329–337.e324 (2019).
78. Aran, D. et al. Reference-based analysis of lung single-cell sequencing reveals a transitional profibrotic macrophage. *Nat. Immunol.* **20**, 163–172 (2019).
79. An integrated encyclopedia of DNA elements in the human genome. *Nature* **489**, 57–74 https://doi.org/10.1038/nature11247 (2012).
80. Szabo, P. A. et al. Single-cell transcriptomics of human T cells reveals tissue and activation signatures in health and disease. *Nature Commun.* **10**, https://doi.org/10.1038/s41467-019-12464-3 (2019).
81. Finak, G. et al. MAST: a flexible statistical framework for assessing transcriptional changes and characterizing heterogeneity in single-cell RNA sequencing data. *Genome Biol.* **16** https://doi.org/10.1186/s13059-015-0844-5 (2015).
82. Gu, Z., Eils, R. & Schlesner, M. Complex heatmaps reveal patterns and correlations in multidimensional genomic data. *Bioinformatics* **32**, 2847–2849 (2016).
83. Gao, C.-H., Yu, G. & Cai, P. ggVennDiagram: an Intuitive, Easy-to-Use, and Highly Customizable R Package to Generate Venn Diagram. *Front. Genet.* **12**, https://doi.org/10.3389/fgene.2021.706907 (2021).
84. Korotkevich, G. et al. *Fast gene set enrichment analysis* (Cold Spring Harbor Laboratory, 2016).
85. Luo, W. & Brouwer, C. Pathview: an R/Bioconductor package for pathway-based data integration and visualization. *Bioinformatics* **29**, 1830–1831 (2013).
86. Jin, S. et al. Inference and analysis of cell-cell communication using CellChat. *Nature Commun.* **12**, https://doi.org/10.1038/s41467-021-21246-9 (2021).
87. Davis, D., Wizel, A. & Drier, Y. *Accurately estimating pathway activity in single cells for clustering and differential analysis* (Cold Spring Harbor Laboratory, 2023).
88. Trapnell, C. et al. The dynamics and regulators of cell fate decisions are revealed by pseudotemporal ordering of single cells. *Nat. Biotechnol.* **32**, 381–386 (2014).
89. Street, K. et al. Slingshot: cell lineage and pseudotime inference for single-cell transcriptomics. *BMC Genom.* **19**, https://doi.org/10.1186/s12864-018-4772-0 (2018).
90. Van Den Berge, K. et al. Trajectory-based differential expression analysis for single-cell sequencing data. *Nature Commun.***11**, https://doi.org/10.1038/s41467-020-14766-3 (2020).
91. R Core Team. R: A language and environment for statistical computing. R Foundation for Statistical Computing, Vienna, Austria. URL https://www.R-project.org/ (2021).
92. GraphPad Prism version 10.0.0 for Windows, GraphPad Software, Boston, Massachusetts USA, www.graphpad.com.

Acknowledgements

We would like to acknowledge all lab members of the Rengarajan lab at Emory University, Elena Morales (clinical research coordinator), and the study participants. We would like to acknowledge Emory I3 NEXUS (Jyothi Rengarajan) seed grant from the Emory University School of Medicine, P30AI168386, for funding and support. Next-generation sequencing services were provided by the Emory NPRC Genomics Core, which is supported in part by NIH P51 OD011132. Sequencing data was acquired on an Illumina NovaSeq 6000 funded by NIH S10 OD026799.

Author contributions

Conceptualization, K.K., P.B., H.K.D., C.I., S.K.C., and J.R.; Methodology, K.K., P.B., C.I., H.K.D., A.B.E., and J.R.; Investigation, K.K., P.B., C.I., H.K.D., A.B.E., S.D., S.K.C, and J.R.; Validation, K.K., S.D., and J.R.; Data Analysis and visualization, P.B., K.K., and J.R.; Resources S.K.C., and J.R.; Writing—original paper, K.K., P.B., and J.R.; Writing—Review & Editing, K.K., P.B., C.I., H.K.D., A.B.E., S.D., S.K.C, and J.R.; Supervision, S.K.C., and J.R.; Funding Acquisition, S.K.C., and J.R.

Competing interests

The authors declare no competing interests.

Additional information

Supplementary information The online version contains supplementary material available at https://doi.org/10.1038/s41467-025-57668-y.

Correspondence and requests for materials should be addressed to Sushma K. Cribbs or Jyothi Rengarajan.

Peer review information *Nature Communications* thanks Janice Endsley and the other anonymous reviewer(s) for their contribution to the peer review of this work. A peer review file is available.

Reprints and permissions information is available at http://www.nature.com/reprints

Publisher's note Springer Nature remains neutral with regard to jurisdictional claims in published maps and institutional affiliations.

Open Access This article is licensed under a Creative Commons Attribution-NonCommercial-NoDerivatives 4.0 International License, which permits any non-commercial use, sharing, distribution and reproduction in any medium or format, as long as you give appropriate credit to the original author(s) and the source, provide a link to the Creative Commons licence, and indicate if you modified the licensed material. You do not have permission under this licence to share adapted material derived from this article or parts of it. The images or other third party material in this article are included in the article's Creative Commons licence, unless indicated otherwise in a credit line to the material. If material is not included in the article's Creative Commons licence and your intended use is not permitted by statutory regulation or exceeds the permitted use, you will need to obtain permission directly from the copyright holder. To view a copy of this licence, visit http://creativecommons.org/licenses/by-nc-nd/4.0/.

© The Author(s) 2025